Nano Today 14 (2017) 42–58

Contents lists available at ScienceDirect

Nano Today

journal homepage: www.elsevier.com/locate/nanotoday

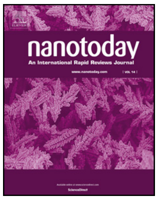

Review

Water splitting dye-sensitized solar cells

Pengtao Xu, Nicholas S. McCool, Thomas E. Mallouk*

Departments of Chemistry, Biochemistry and Molecular Biology, and Physics, The Pennsylvania State University, University Park, PA 16802, USA

ARTICLE INFO

Article history:
Received 6 January 2017
Received in revised form 4 March 2017
Accepted 24 April 2017
Available online 15 May 2017

Keywords:
Dye-sensitized solar cell
Photoelectrochemical cell
Solar fuels
Artificial photosynthesis
Water splitting
Molecular sensitizer

ABSTRACT

Research in artificial photosynthesis is driven by the goal of creating low-cost, integrated systems for the direct conversion of solar energy to high energy density fuels. Water-splitting dye-sensitized solar cells can in principle leverage the successful architecture, spectral tunability, and high quantum efficiency of regenerative photovoltaic dye cells toward this goal. In this article, we review the current development of both dye-sensitized photoanodes and photocathodes for water splitting. A detailed discussion of the individual components of photoanodes and photocathodes – semiconductors, sensitizers, and catalysts – is presented. We review experiments on the electron transfer kinetics that control the efficiency of water splitting, and highlight recent research on electrode architectures that can improve both the efficiency and stability of water-splitting dye cells.

Contents

Introduction

Solar energy conversion has the potential to provide a practically limitless source of renewable and clean energy. Although in past decades solar power could not compete on a cost basis with electricity generation from fossil fuel, nuclear, or hydroelectric sources, the cost of photovoltaic modules has steadily dropped since the 1970s at an average rate of about 15% per year [1]. As inexpensive photovoltaics achieve grid parity in more and more of the developed world, they will bring about sweeping changes in the way electricity is produced, distributed, and used. At present, electricity production accounts for about 39% of primary energy use in the United States, which is mostly derived from fossil fuel resources. The remaining 61% of the U.S. energy economy, which is dominated by the transportation and industrial sectors, relies heavily on fossil fuels. All together the combustion of fossil fuels accounts for about 80% of the world’s energy economy [2]. Better energy storage technologies have the potential to shift the balance of energy use toward electricity [3,4], but the need for combustible fuel will be

---

* Corresponding author.
E-mail address: tem5@psu.edu (T.E. Mallouk).

http://dx.doi.org/10.1016/j.nantod.2017.04.009
1748-0132/

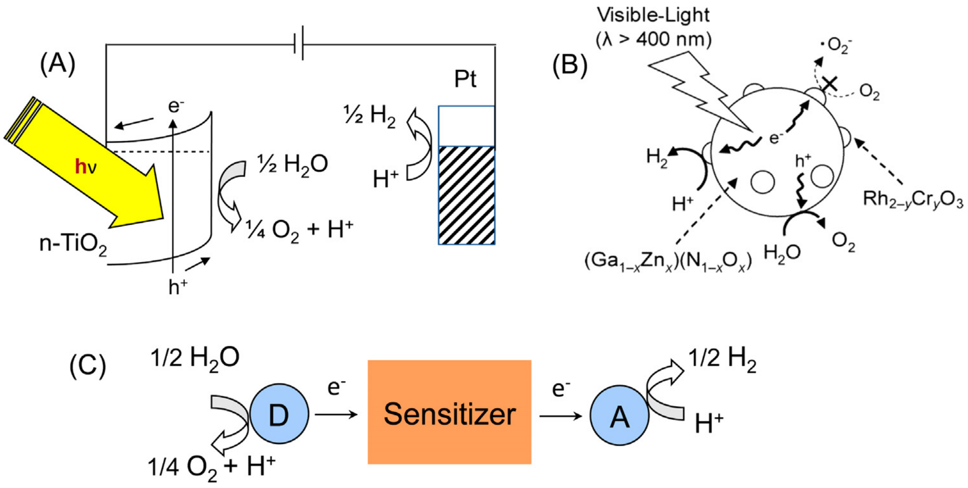

Fig. 1. Solar fuel production by (a) semiconductor photoelectrochemistry, e.g., in the Fujishima-Honda cell [16], (b) photocatalysis, e.g., at a Rh-catalyzed $Ga_{1-x}Zn_xN_{1-x}O_x$ particle (adapted with permission from Ref. [17], Copyright 2006 John Wiley & Sons, Inc.), and (c) artificial photosynthesis in a sensitizer-donor (D)–acceptor (A) system [18].

with us for some time for transportation, heating, manufacturing, and many other uses.

The electrolysis of water to produce hydrogen is a mature technology, and hydrogen derived from photovoltaic power can be used directly or combined catalytically with CO_2 to make high energy density liquid fuels. While the energy efficiency of electrolyzers is high, their capital cost limits the commercial viability of power-to-gas technologies [5]. Additionally, cost targets for solar fuels are much more challenging than they are for solar electricity. Solar electricity can compete with power generation from fossil fuels because the latter process is inherently inefficient due to Carnot cycle losses. However, fuel derived from solar energy must compete directly with the heating value of fossil fuel, meaning that cost parity of commodity fuels with hydrogen from photovoltaic-electrolyzer systems would require a substantial lowering of electrolyzer cost.

An alternative pathway to solar fuels involves the direct production of fuel through photocatalysis or photoelectrochemistry (see Fig. 1). Although none of these schemes are yet technologically viable, they could potentially offer a low-cost alternative to a stand-alone electrolyzer by coupling catalytic fuel generation directly to the light absorber. In these systems, light is absorbed by a molecule or semiconductor, electrons and holes are separated over short distances – typically nanometers to microns – and chemical reactions occur at solid–liquid or solid–vapor interfaces. Most typically, the reaction of interest is water splitting, but there has also been growing interest in the photochemical splitting of CO_2 to carbon-containing fuels and oxygen [6–11], the light-driven reverse water gas shift reaction ($CO_2 + H_2 = CO + H_2O$) [12,13], and the reaction of nitrogen with water to produce ammonia and oxygen [14,15].

In principle, the three kinds of solar fuel systems shown in Fig. 1 are all subject to the same thermodynamic limit of ~33% efficiency [19,20], and better utilization of the solar spectrum can be achieved if two light absorbers are arranged in series (as they are in natural photosynthesis) to drive the energetically demanding water splitting reaction [21,22]. In practice, some energy must be given up for catalytic hydrogen and oxygen evolution to proceed at useful rates, and some energy is lost to series resistance. If these combined losses (along with membrane polarization losses [23,24]) do not exceed about 1.0 V, then power conversion efficiencies of 10–15% can in principle be achieved [21], and in fact have been demonstrated in model systems [25–28]. A recent techno-economic analysis of photocatalytic and photoelectrochemical solar fuel systems suggests that they can be economically viable at power conversion efficiencies above about 10% [29]. It is important to recognize from these analyses however that solar fuel performance targets can be met only if the *quantum* efficiency (the fraction of photons that produce current or a chemical reaction) is close to unity. Although much progress has been made toward achieving this goal in photovoltaic-electrolyzer systems, most semiconductor-based photoelectrochemical systems (Fig. 1a) are poorly matched to the solar spectrum or are unstable in water, and photocatalysts (Fig. 1b) typically have low quantum yields because of uncontrolled charge recombination. Recent reviews describe these challenges and the extensive work that has been done to address them [30,31]. Here we focus instead on fledgling molecule-based water-splitting systems (Fig. 1c). Although they are at a primitive stage of development technologically, in principle molecule-based (or artificial photosynthetic) systems offer flexibility in the design of molecular light absorbers to cover the full solar spectrum, and they can take advantage of the high quantum yield of light-driven charge separation that has already been achieved at dye-semiconductor interfaces.

Dye sensitized solar cells: regenerative and photosynthetic

Because molecular water splitting cells are currently based on the architecture of the dye-sensitized solar cell (DSSC), it is important to review the basic operating principles of the latter. The DSSC (also known as the Grätzel cell) is a regenerative photoelectrochemical cell, i.e., a liquid-junction cell in which the anode and cathode reactions are the reverse of each other. The DSSC utilizes high surface area electrodes – typically ~10 μm-thick films of anatase TiO_2 nanoparticles – to adsorb a monolayer of dye, which sufficiently harvests most of the incident light. Early designs of DSSCs used aqueous electrolytes [32], but a breakthrough came in 1991 when O'Regan and Grätzel introduced non-aqueous iodide-based dye cells [33]. Subsequent optimization of dyes, light scattering layers, electrode blocking layers, and the redox couple in non-aqueous DSSCs have resulted in quantum efficiencies close to unity over much of the visible spectrum and champion cell solar-to-electric power conversion efficiencies as high as 14.1% [34].

The DSSC is compared to an early design of the water-splitting dye cell in Fig. 2. In the water-splitting version, an aqueous electrolyte is used, and a catalyst for the oxygen evolution reaction (OER) – either a catalytic nanoparticle or a molecular catalyst that is bound to or co-adsorbed with the sensitizer – replaces the iodide/triiodide redox shuttle in the DSSC. Oxygen is evolved at the dye-sensitized photoanode and water is reduced to hydrogen at a dark catalytic cathode. Because the photoinjected electrons in the anatase film are not sufficiently reducing to generate hydrogen

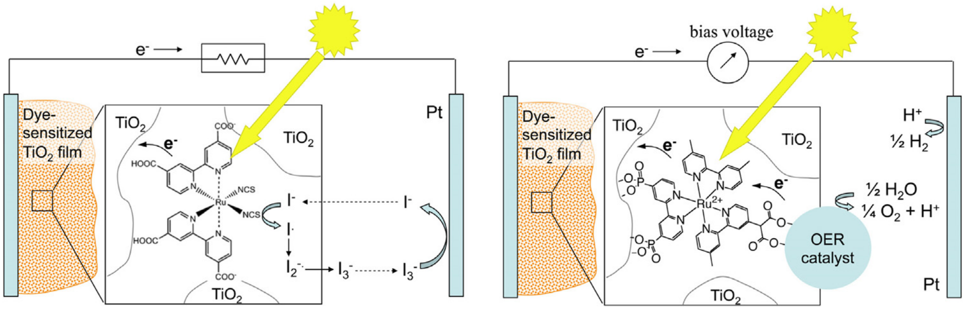

Fig. 2. The architecture of regenerative (left) and water-splitting (right) DSSCs. The regenerative DSSC is fabricated as a sandwich cell with a short (~100 μm) electrolyte path between the photoanode and dark cathode. In the water-splitting cell, the anode and cathode are typically separated by a membrane or frit (not shown) in order to enable separation of photogenerated oxygen and hydrogen. Adapted with permission from Ref. [35]. Copyright 2009 American Chemical Society.

from water, a minimum cathodic bias of 200–300 mV is needed, as in the original Fujishima-Honda cell [16] and other water splitting cells based on visible light-absorbing anode materials such as Fe_2O_3, WO_3, and $BiVO_4$ [36–40]. Thus the water splitting dye cell can be thought of as a hybrid of the Fujishima-Honda cell and the Grätzel cell.

The relevant electrochemical potential diagrams for these three kinds of solar cells are shown schematically in Fig. 3. In the Fujishima-Honda cell and related cells based on wide bandgap oxide semiconductor electrodes, light absorption creates strongly oxidizing valence-band holes that rapidly oxidize water. The internal quantum yield for water oxidation can be high, especially at high bias where electrons and holes are efficiently separated, but utilization of the solar spectrum is poor. In the DSSC, the quantum yield is also high, a consequence of sub-picosecond electron injection from the photoexcited dye into the TiO_2 conduction band, followed by reduction of the oxidized dye by iodide on the nanosecond timescale. Dye reduction by iodide is orders of magnitude faster than back electron transfer from TiO_2 to the oxidized dye, and because back electron transfer to I_3^- is also slow [41], the forward electron transfer pathways dominate over the reverse pathways. In contrast, in the water-splitting DSSC, catalytic water oxidation is typically slow (millisecond timescale) because of the weak driving force for the reaction. While the millisecond turnover rates of the best water oxidation catalysts are adequate to sustain water electrolysis at 1 sun irradiance ($j \sim 20\,mA/cm^2$), they are too slow to compete effectively with back electron transfer on the 100 s of microseconds timescale (Fig. 3c). Low quantum yields for water splitting – typically 1–2% – are a consequence of the fast kinetics of charge recombination, which competes effectively with the catalytic oxidation of water. Since the introduction of the water splitting dye cell in 2009, much of the effort in re-design of the photoanode has focused on improving the quantum yield by slowing down back electron transfer and/or accelerating the water oxidation process.

Dye-sensitized photoanodes for water-splitting cells

Electron and proton transfer at dye-sensitized photoanodes

Because of its importance in aqueous electrochemical systems, the catalytic four-electron oxidation of water to oxygen has been well studied and many different OER catalysts have been developed. Following the initial demonstration of visible-light water splitting in a DSSC (using colloidal $IrO_x{\cdot}nH_2O$ covalently bound to the sensitizer molecule, Fig. 2) [35], a number of groups have tested different colloidal and molecular water oxidation catalysts in similar electrode architectures. The results are summarized in Table 1.

These experiments revealed interesting similarities in the electrochemical behavior of photoanodes – fabricated from different dyes and catalysts – that were initially difficult to rationalize (Fig. 6). When the photoanodes were abruptly irradiated with simulated sunlight, the initial photocurrent densities were in the range of 15–200 μA/cm^2, but they decayed over a timescale of tens of seconds to a fraction of their initial value. Interestingly, dye decomposition or desorption could be ruled out as the principal source of photocurrent decay because most of the initial photocurrent could be recovered after switching the light off for a few seconds.

Generator-collector experiments showed that despite the transient nature of the photocurrent, the Faradaic efficiency of oxygen evolution was close to unity [48,52]. Electrodes that were tested in a regenerative DSSC architecture (i.e., in non-aqueous iodide solutions) gave an order of magnitude higher current density and showed minimal photocurrent decay [47].

The kinetic origin of the low quantum yield and transient nature of the photocurrent in water-splitting dye cells was clarified through a series of spectroelectrochemical and transient spectroscopy experiments [52,73–75]. The detailed kinetic framework was adapted from earlier studies of the DSSC [76], and is illustrated schematically in Fig. 7.

Electrodes fabricated with sintered IrO_2 catalysts (Fig. 7) enabled systematic studies of electron transfer processes as a function of the dye coverage, catalyst loading, solvents used to adsorb the dye, and incident light intensity. Following photoinjection of electrons by dye molecules, holes diffuse across the surface to reach the IrO_2 catalyst. The regeneration of reduced dye molecules occurs in competition with charge recombination and electron scavenging by Ir(IV). The cross-surface diffusion coefficient (D_{app}) was measured by a spectroelectrochemical potential step method [77], and charge recombination (k_{recomb}) and electron scavenging (k_{scav}) rate constants were obtained from transient photovoltage measurements. Interestingly, the photocurrent for water splitting was strongly dependent on the solvent and conditions used to adsorb the dye. Exposure of the electrodes to acidic, aqueous solvents resulted in low photocurrents despite relatively high values of D_{app}. Spectroelectrochemical and electrochemical impedance measurements showed that intercalated protons helped to trap photoinjected electrons at sites where they could readily combine with oxidized dye molecules [74], consistent with previous studies of proton intercalation in nanoporous TiO_2 films [78].

The impact of proton-induced trap states on electron transfer at dye-sensitized TiO_2 photoanodes was recently studied by McCool et al. [75] using transient absorption spectroscopy (TAS) and time-resolved terahertz spectroscopy (TRTS). Lower electron injection yield from TRTS and faster back electron transfer rates from TAS were found for photoanodes sensitized from perchloric acid, relative to those sensitized from anhydrous ethanol. This contrast implies the formation of trap states during exposure to protic sol-

Table 1
Photoanode sensitizers and assemblies for water-splitting dye cells.

Reference	Semiconductor	Dye	OER catalyst	Steady-state photocurrent (μA/cm^2)	Faradaic efficiency of O_2 generation	Photocurrent stability (h)	IPCE (wavelength)	Photocurrent test conditions
[35]	TiO_2	RuP2	$IrO_2 \cdot nH_2O$	10–30 (0.58 V)	20%	4	0.5% (450 nm)	Xe lamp (>410 nm), pH 5.75
[42]	TiO_2	RuC1	$[Mn_4O_4L_6]^{+}$[a]	3–15 (0 V vs. Pt)[b]	93%	2	1.7% (430 nm)	Xe lamp (100 mW/cm^2, 290–750 nm), pH 7 (no buffer)
[43]	TiO_2	RuP1	Ru1	40 (0 V vs. Pt)[b]	n/a	1	n/a	White light emitting diode array (100 mW/cm^2), pH 7 (no buffer)
[44]	TiO_2	ZnPor	Ir1	30 (0.91 V)	n/a	n/a	n/a	White light (~200 mW/cm^2, >400 nm pH7 no buffer)
[45]	TiO_2	Poly-heptazine	$IrO_2 \cdot nH_2O$	120 (1.12 V)	n/a	1.5	n/a	Xe lamp (>420 nm), pH7
[46]	TiO_2	Poly-heptazine	Co-Pi	75 (1.0 V)	n/a	3	5.5% (350 nm)	450 nm, pH7
[47]	TiO_2/Nb_2O_5	RuP2	$IrO_2 \cdot nH_2O$	15–20 (0.55 V)	109%	n/a	n/a	Xe lamp (100 mW/cm^2, >410 nm), pH 5.75
[48]	TiO_2	RuP3	IrOx nanoparticles	80 (0.55 V)	85%	n/a	5% (450 nm, estimated)	Xe lamp (>410 nm), pH 5.8
[49]	TiO_2	RuP1	$\{Ru_4O_4(OH)_2(H_2O)_4\}[(\gamma\text{-}SiW_{10}O_{36})_2]^{10-}$	15 (0.55 V)	n/a	0.33	0.20%	Xe lamp (420–470 nm, 30 mW/cm^2), pH 5.8
[50]	TiO_2	RuP1	Ru4	1700 (0.60 V)	83%	n/a	14% (450 nm)	Xe lamp (>400 nm, 300 mW/cm^2), pH 6.8
[51]	*nano*ITO/TiO_2	RuP9-Ru8		80 (0.47 V)	n/a	0.5	4.4% (445 nm)	LED (72.5 mW/cm^2, 445 nm), pH 4.5
[52]	TiO_2	RuP1	Sintered IrO_2	80 (0.70 V)	98%	n/a	2.4% (410–700 nm)	Xe lamp (>410 nm), pH 6.8
[53]	TiO_2	RuP1	Ru2-1, Ru2-3	1400 with Ru2-3, 700 with Ru2-3 (0.58 V)	n/a	n/a	n/a	Xe lamp (>400 nm, 300 mW/cm^2), pH 6.4
[54]	TiO_2	RuP4	Ru3	480 (0.58 V)	n/a	n/a	4.1% (450 nm)	Xe lamp (>400 nm, 300 mW/cm^2), pH 6.4
[55]	n/a	PMPDI	CoOx	150 (1.61 V)	80 ± 15%	n/a	0.12% (475 nm)	Xe lamp (315–710 nm, 100 mW/cm^2), pH 7
[56]	TiO_2	RuP1	Ru4	40 (0 V vs. Pt)[b]	73.80%	0.23	1.85% (455 nm)	Xe lamp (>400 nm, 100 mW/cm^2), pH 6.4
[57]	SnO_2	PPor	Ir1	50 with PPor, 20 with PPor + Ir1 (0.92 V)	n/a	n/a	n/a	White light (~200 mW/cm^2, >400 nm pH 7 no buffer)
[58]	TiO_2	RuP5	$[\{Ru_4O_4(OH)_2(H_2O)_4\}(\gamma\text{-}SiW_{10}O_{36})_2]^{10-}$	54.8 (0.55 V)	86%	5	0.392%[c]	LED light (455 nm, 33 mW/cm^2), pH 5.8,
[59]	TiO_2	Poly-heptazine	Co(II) ion	90 (1.06 V)	38.60%	1	n/a	Xe lamp (>420 nm), pH 6
[60]	TiO_2	RuP1	Ru9	20 (1.16 V)	16.80%	6	n/a	White light (~200 mW/cm^2, >380 nm), pH 8.8
[61]	TiO_2	TMP, DMP, MMP, TTP, PAP, DMEP, MDC, MDCE	Citrate-capped IrO_x	15 (0.71 V)	102 ± 5%	n/a	<0.05%	Xenon lamp (>410 nm or >590 nm), pH 6.8
[62]	SnO_2/TiO_2	RuP9-Ru8		100 (0.6 V vs. Pt)[b]	41%	0.42	n/a	LED light (445 nm, 46.2 mW/cm^2), pH 7
[63]	TiO_2	L0	Ru10	300 (0.62 V)	73%	1	n/a	White LED (>400 nm, 100 mW/cm^2), pH 7
[64]	SnO_2/TiO_2	RuP8-Ru1		300 (0.95 V)	22%	0.5	3.75% (435 nm)	White LED light (100 mW/cm^2, >400 nm), pH 7
[65]	*nano*ITO/TiO_2	RuP7	IrO_x nanoparticle	150 (0.54 V)	n/a	2	n/a	LED light (450 nm, 14.5 mW/cm^2), pH 5.8
[66]	SnO_2/TiO_2	TPA	Ru7	100 (0.85 V)	8.2%	n/a	n/a	White light (>400 nm, 100 mW/cm^2), pH 7
[67]	TiO_2	RuP1	Ru5	1200 (0.60 V)	81%	n/a	9.5% (450 nm)	White light (300 mW/cm^2, >400 nm), pH 6.8
[68]	TiO_2	ZnPor-Ru1		100 (0.23 V)	33%	1	17% (424 nm) 5.9% (564 nm)	White light (35 mW/cm^2, >380 nm), pH7.3
[69]	TiO_2	RuP6	Ru6	800 (0.61 V)	72%	n/a	7% (460 nm)	Xe lamp (300 mW/cm^2, >400 nm), pH 7 with 5% CF_3CH_2OH
[70]	SnO_2/TiO_2	RuPS	Ru8	10 (0.85 V)	22%	n/a	n/a	White light (100 mW/cm^2, >400 nm), pH 7
[71]	SnO_2/TiO_2	RuP9-Ru1		850 (0.63 V)	74%	n/a	n/a	White light (100 mW/cm^2), pH5.7
[72]	SnO_2/TiO_2	RuP8-Ru11		400 (1.06 V, pH 7) 500 (1.17 V, pH 9)	30% (pH 7) 45% (pH 9)	n/a	n/a	White light (100 mW/cm^2, >400 nm)

See Figs. 4 and 5 for structure codes.

Steady-state current and stability data are from chronoamperometry experiments (typically recorded after 10–30 s of illumination). Potentials in bracket are the applied potential vs. RHE unless otherwise noted. Potential conversion follows these equations except where the reference potential is given in the original paper:

a $E(\text{V vs. RHE}) = E(\text{V vs. Ag/AgCl 3 M KCl/NaCl}) + 0.210 + 0.0592 \times \text{pH}$.

b $E(\text{V vs. RHE}) = E(\text{V vs. Ag/AgCl sat.}) + 0.197 + 0.0592 \times \text{pH}$.

c $E(\text{V vs. RHE}) = E(\text{V vs. SCE}) + 0.241 + 0.0592 \times \text{pH}$.

d $E(\text{V vs. RHE}) = E(\text{V vs. NHE}) + 0.0592 \times \text{pH}$.

Eq. (1) was used when Ag/AgCl filling solution is not indicated.

Stability duration results are tabulated based on the longest test time $> 10\,min$ indicated in the literature.

[a] L = bis(methoxyphenyl)phosphonate.

[b] Measurement was done in a two-electrode configuration.

[c] Internal quantum efficiency.

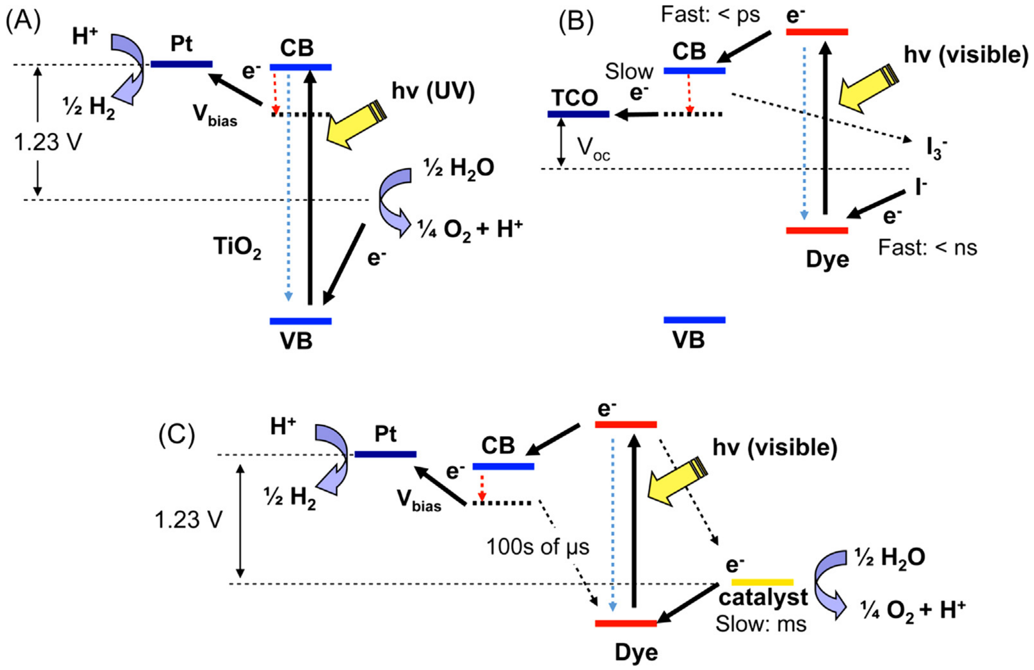

Fig. 3. Electrochemical potential diagrams for (a) Fujishima-Honda, (b) Grätzel, and (c) water-splitting dye-sensitized solar cells. Solid lines indicate forward electron transfer pathways. Charge recombination pathways are shown as dashed lines.

vents. Although these trap states can be temporarily removed when the electrodes undergo mild heating (80 °C) under vacuum [75], proton intercalation can still occur slowly during photoelectrolysis [73].

Using rate constants from transient photovoltage measurements, Swierk et al. were able to construct a kinetic model (Eq. (1)) that could accurately fit the photocurrent transients observed with the water-splitting dye cell.

$$\frac{\partial n_t}{\partial t} = G - k_{detrap} e^{-\frac{E_c - E_t}{kT}} (N_{cb} - n_{cb}) n_t - k_{recomb} n_{Ru^{3+}} n_t - k_{scav} n_{Ir^{4+}} n_t \quad (1)$$

In this equation n_t and n_{cb} are the densities of trapped and conduction band electrons, G is the electron generation rate (which is proportional to the light flux), $n_{Ru^{3+}}$ and $n_{Ir^{4+}}$ are the densities of oxidized dye molecules and electron scavenger sites, N_{cb} is the total density of conduction band states, and E_c and E_t are conduction band edge and trap energies, respectively. Representative data and fits are shown in Fig. 8, along with a plot of $n_{Ru^{3+}}$ and n_t as a function of irradiation time. The model shows that the photocurrent (which is proportional to n_{cb}) decays over a period of tens of seconds as $n_{Ru^{3+}}$ and n_t increase, eventually reaching a photostationary state.

It is clear from this analysis that strategies that can lower k_{recomb} or accelerate D_{app} or k_{trans} should improve the efficiency of water splitting. The recombination rate can be lowered by increasing the distance between the sensitizer and electron trap sites, or by preventing proton intercalation. Indeed, the most efficient cells reported, which have quantum efficiencies of ~15% and photocurrent densities of 2–3 mA/cm^2 [50,54], embody some of these strategies. Gao et al. demonstrated that the photocurrent increases with increasing pH [50], and Zhao et al. showed that higher steady-state current could be obtained by incorporating an electron transfer mediator between the sensitizer and catalyst sites [48].

Core–shell photoanode architectures

As noted above, lowering the back electron transfer rate from the semiconductor to the oxidized sensitizer molecule on its surface should increase the quantum efficiency of oxygen evolution in water-splitting dye cells. Two kinds of core/shell structures have been fabricated and tested in water-splitting dye cells. In the first type, the shell is applied before the sensitizer is adsorbed, and in the second, the adsorbed sensitizer is covered by the shell material (Fig. 9). While the first type is primarily targeted toward slowing down back electron transfer, the second type of core–shell structure seeks to address the issue of dye stability.

Core–shell-sensitizer architectures

In solid-state semiconductor solar cells, an insulating layer between the metal top contact and the semiconductor is often used to inhibit interfacial charge recombination [79]. This strategy has been adapted to the DSSC by using a conformal coating of insulating overlayers on the surface of the mesoporous oxide semiconductor [80–82]. The difference in conduction band edge potentials at the core–shell interface creates an energy barrier for charge recombination, and thus increases the charge transfer efficiency, although thicker shells may lower the effective surface area for dye loading. The concept of using core–shell electrodes has recently been applied to water splitting dye cells, where improved electron transfer kinetics have been reported [47,51,64–66].

Lee et al. [47] reported RuP2-sensitized TiO_2/ZrO_2 and TiO_2/Nb_2O_5 core–shell photoanodes prepared by surface sol-gel deposition of the wide bandgap oxide. TAS showed that back electron transfer from the semiconductor to the oxidized dye was slowed by a factor of 2–3. Incorporation of the insulting layer was also found to increase the photocurrent of the photoanode. However, the ZrO_2 and Nb_2O_5 films prepared by this method were not uniform and uncoated areas could be seen using high-resolution transmission electron microscopy (TEM). More conformal core–shell electrode films were later reported by the Meyer group using atomic layer deposition (ALD) [51,62,65].

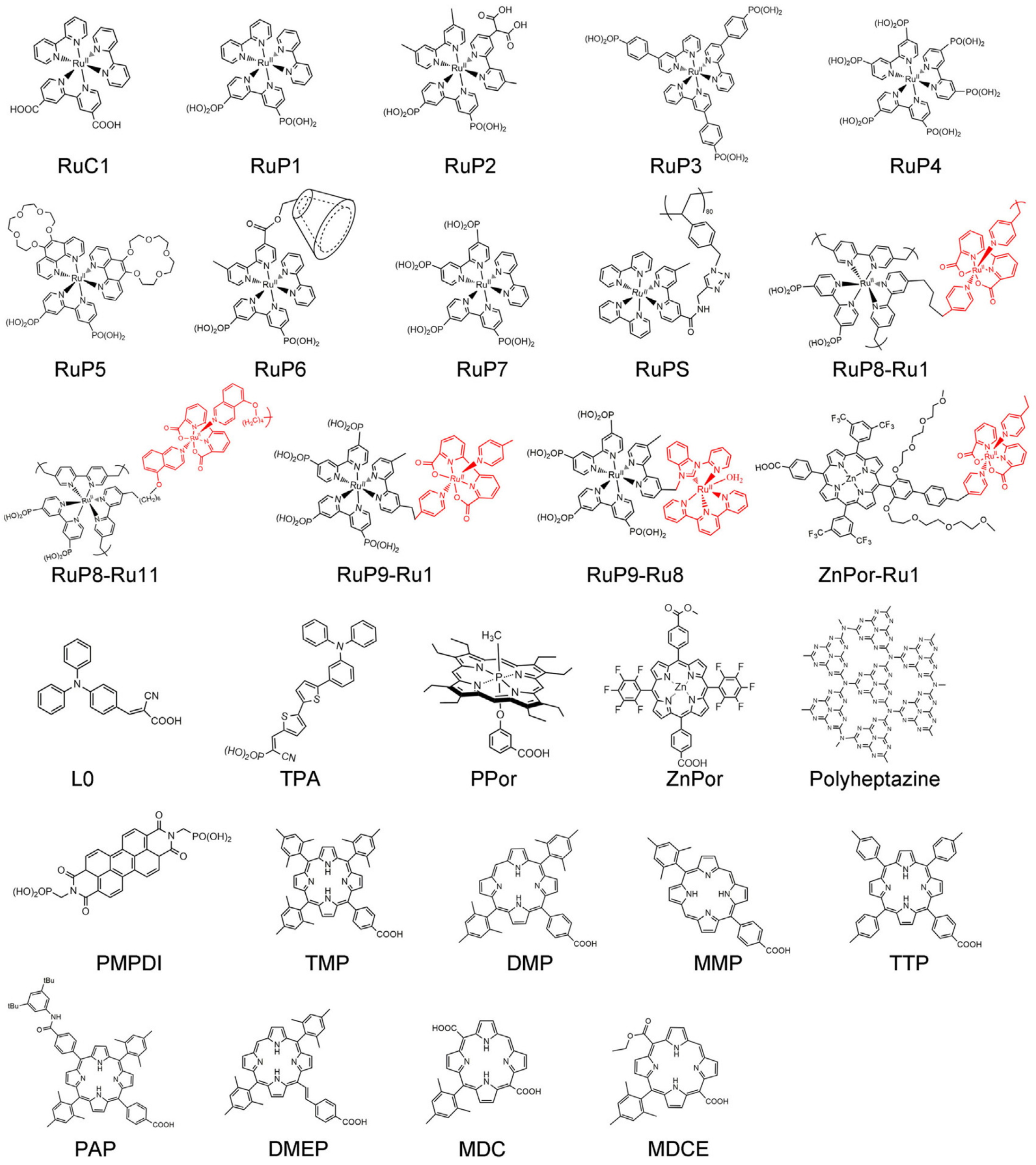

Fig. 4. Sensitizers and sensitizer-catalyst assemblies (catalysts are colored red) that have been used in dye-sensitized photoanodes. See Table 1 for references. (For interpretation of the references to color in this figure legend, the reader is referred to the web version of the article.)

Instead of using TiO_2 as the core material, they used tin-doped indium oxide in its nanoparticle form (*nano*ITO) as a conductive mesoporous support, with the TiO_2 shell material prepared by ALD. This *nano*ITO/TiO_2 core–shell electrode, when sensitized with RuP7 and IrO_x nanoparticles, gave higher photocurrent relative to mesoporous TiO_2 electrodes [65]. Further improvement was achieved with sensitized SnO_2/TiO_2 photoanodes. Testing under the same conditions with the RuP9-Ru8 chromophore-catalyst assembly, Alibabaei et al. [62] reported that the photocurrent from the *nano*ITO/TiO_2 core–shell photoanode was one-fifth that of the SnO_2/TiO_2 photoanode. One explanation is that back-electron transfer tunneling through the TiO_2 layer is still a competing process with *nano*ITO/TiO_2 electrodes [83]. Using co-sensitization of TPA and Ru7, Wee et al. [66] compared the performance of mesoporous TiO_2 electrodes and SnO_2/TiO_2 (3 nm) core–shell electrodes. TAS experiments showed that back electron transfer from the core/shell structure was more than five times slower than from the TiO_2 photoanode. A profound difference was also found in photocurrent measurements with hydroquinone as the hole scavenger; the core–shell electrode sustained a photocurrent of ~2.5 mA/cm^2 compared to ~5 $\mu A/cm^2$ from the TiO_2 electrode.

Enabled by the precise control of the film thickness with ALD, research has been done to study the impact of the shell thickness on electron transfer rates in core–shell assemblies [84–86]. It is important to note that the ALD thickness indicated in the literature is usually determined by monitoring film growth on a silicon wafer inside the ALD chamber. This value may not reflect the actual coating thickness on the sample, because the rate of ALD film growth depends strongly on the substrate, especially the nucleation of the precursor on the surface in the first few cycles [87].

Using time-resolved terahertz spectroscopy (TRTS) to probe the electron injection dynamics in a dye-sensitized SnO_2/TiO_2 core–shell assembly, McCool et al. [85,88] observed rapid (within 10 ps) and slower (longer than 100 ps) injection behavior from TRTS signals, which were ascribed to fast injection of electrons into the TiO_2 shell, subsequent relaxation into non-mobile trap states, and

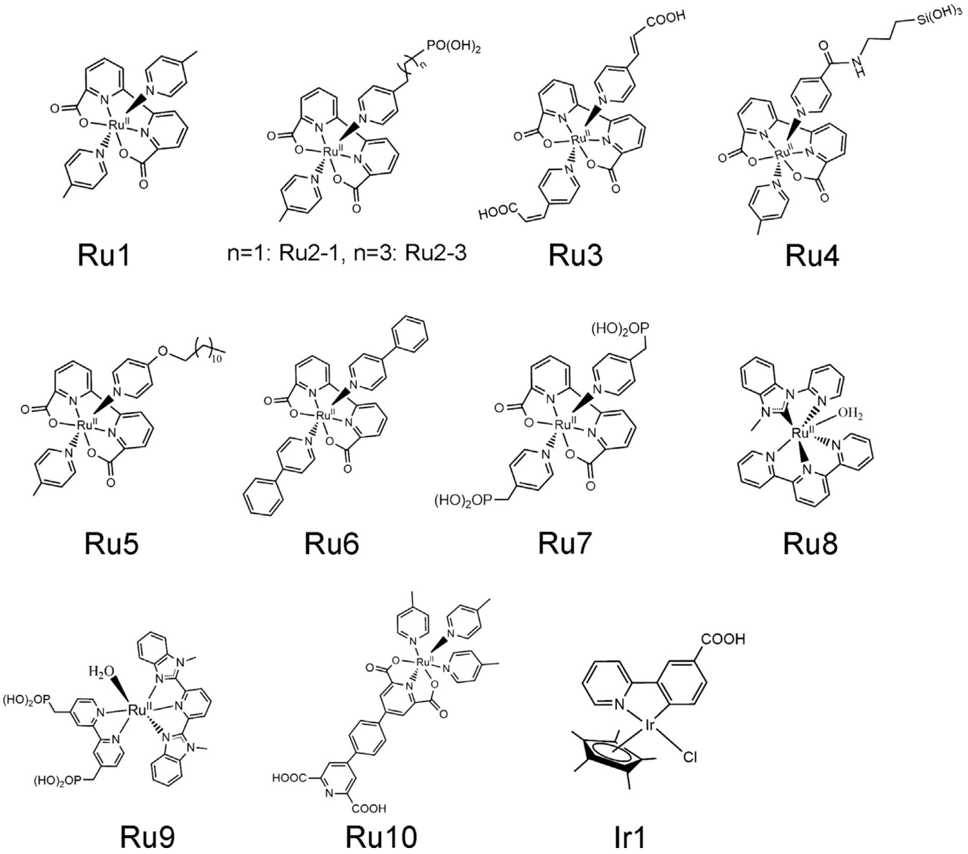

Fig. 5. Molecular OER catalysts used in dye-sensitized water splitting cells. See Table 1 for references.

finally slow release of electrons from the TiO_2 shell into the SnO_2 core (Fig. 10). This two-step injection mechanism was observed for TiO_2 shells of thickness greater than 5 Å. The degree of trapping in the shell increased with increasing shell thickness. When the shell was thinner than 5 Å, direct tunneling of electrons through the TiO_2 shell into the SnO_2 core was found. Interestingly, the observed injection amplitude was found to increase with as few as one or two ALD cycles relative to uncoated SnO_2 electrodes. This increase in charge injection amplitude was most probably due to the passivation of non-mobile surface states by the ALD coating, as suggested in other reports on similar systems [89,90].

While TRTS probes the ultrafast electron injection dynamics within one nanosecond, TAS can provide useful information about charge recombination dynamics on timescales longer than nanoseconds in dye-sensitized core–shell systems. From TAS of RuP1-sensitized SnO_2/TiO_2 core–shell particles, Dempsey and coworkers [84] found that annealing following the ALD process dramatically changed the interfacial charge recombination dynamics despite the improved crystallinity of the shell evidenced by X-ray diffraction (XRD). While the back electron transfer rate through the amorphous (unannealed) shell showed a strong dependence on the shell thickness, charge recombination in the annealed core–shell structure was independent of shell thickness when the shell was thicker than 0.5 nm. They also modeled the back electron transfer rates through amorphous shells of different thickness to determine the contribution of tunneling and direct shell-mediated recombination mechanisms (Fig. 11). With amorphous shells thinner than 3.2 nm, the tunneling mechanism dominated back electron transfer; in contrast, back electron transfer occurred primarily from the TiO_2 shell when shell thickness was greater than 3.2 nm. The SnO_2/TiO_2 core–shell electrodes prepared by McCool et al. [85,88] were annealed prior to the dye sensitization process.

The ultrafast recombination dynamics of SnO_2/TiO_2 core–shell photoanodes were recently reported by Gish et al. [86]. Comparing the excited state absorption and ground-state bleaching signals from femtosecond TAS, they found that back electron transfer to about 60% of the oxidized sensitizer molecules occurred within 1 ns in the core–shell architecture, but the lifetime of the remaining charge-separated states was extended.

"Mummy" photoanodes

The second type of core–shell assembly is formed by insulating the dye-loaded core material with a nm-thick shell of polymeric or semiconducting material. This method of preventing dye desorption has received increased attention in the literature on both conventional and water-splitting DSSCs [62,65,91–97]. When a sensitized mesoporous TiO_2 photoanode is covered with fewer than ten cycles of ALD (i.e., less than 1 nm of an overlayer), the dye stability in aqueous solution increases dramatically. Such electrodes are an order of magnitude more stable than untreated films, even at elevated pH [91,92]. It was proposed (Fig. 12) that the precursor for the shell ($TiCl_4$ for TiO_2, for example) reacts first with the terminal hydroxyl groups on the TiO_2 surface and the anchoring groups of the sensitizer molecules; then, the water pulse in the subsequent ALD step hydrolyzes the remaining Ti–Cl bonds to give hydroxyl termination. Repetition of the alternating $TiCl_4$ and water pulses leads to layer-by-layer growth of an amorphous TiO_2 shell, mummifying the sensitizer molecules. Because of their reactive nature, care has to be taken when selecting organometallic precursors and the oxygen source (e.g. water, ozone) in order to avoid dye degradation [95].

So far, TiO_2 and Al_2O_3 shells grown by ALD have been used to stabilize core-adsorbed sensitizers, and dye desorption rates were

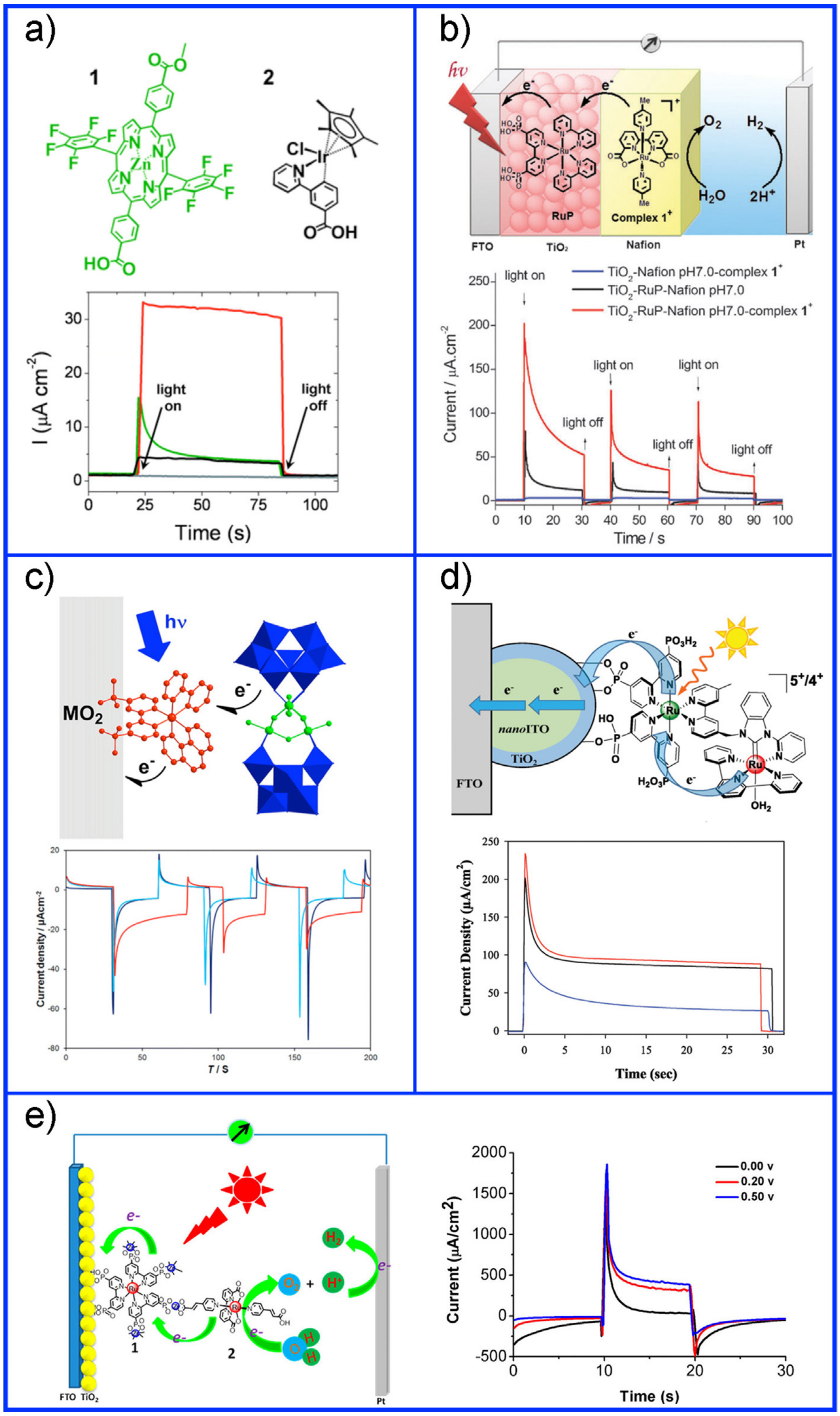

Fig. 6. Photoelectrochemical transients obtained with different dyes and water oxidation catalysts in water-splitting dye cells. Reproduced from Ref. [44] (with permission of The Royal Society of Chemistry), Ref. [43] (with permission of The Royal Society of Chemistry), Ref. [49] (Copyright 2013 American Chemical Society, adapted with permission), Ref. [51], and Ref. [54] (Copyright 2014 American Chemical Society, adapted with permission).

found to be slower with TiO_2 shells than with Al_2O_3 [91]. The addition of these shells was, however, found to reduce the electron injection yield by TAS. In experiments with the RuP1-sensitized TiO_2 core, the emission intensity of the dye decreased with thicker TiO_2 overlayers but increased with thicker Al_2O_3. This suggested that ALD TiO_2 lowered the electron injection yield by introducing new electron acceptor sites in the shell, whereas ALD Al_2O_3 did so by inhibiting excited state electron injection [91]. As a result, the photocurrent measured in short-time tests was decreased relative to uncoated electrodes, but the photocurrent was increased in long-time tests because of increased dye stability (Fig. 13) [60,65]. Alibabaeia et al. [62] compared the photocurrent from RuP9-Ru8-sensitzied SnO_2/TiO_2 core–shell photoanodes with ALD TiO_2 and Al_2O_3 as overlayers for dye stabilization. Higher photocurrent was

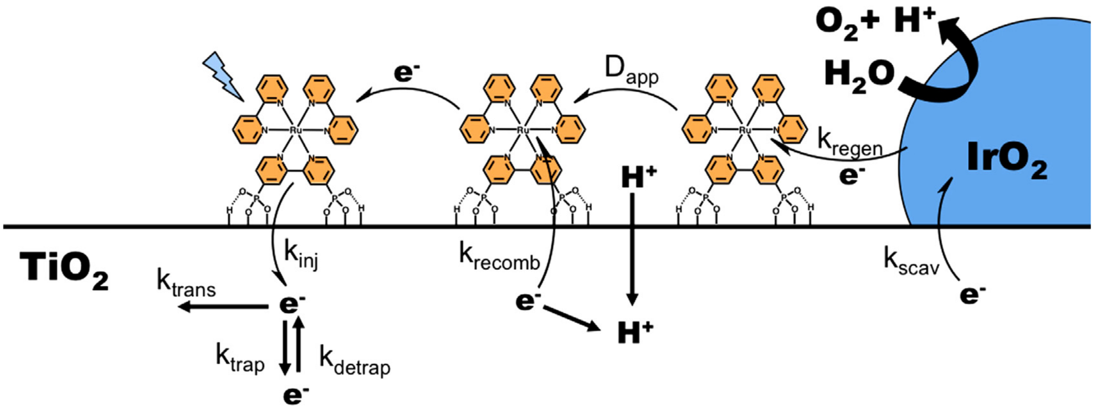

Fig. 7. Kinetic scheme for the photoanode of a water-splitting dye-sensitized solar cell containing an adsorbed molecular sensitizer and a colloidal IrO_2 catalyst sintered to the high surface area anatase TiO_2 film. Reproduced with permission from Ref. [73]. Copyright 2014 American Chemical Society.

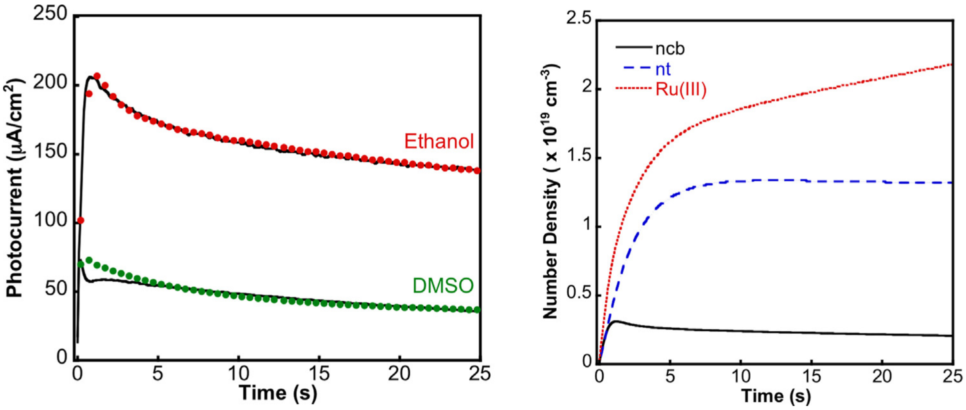

Fig. 8. Left: Photocurrent transients from photoanodes sensitized from DMSO and ethanol solutions. Black lines are fits to Eq. (1). Right: Calculated number density of conduction band electrons (n_{cb}), trapped electrons (n_t), and oxidized sensitizer molecules (Ru(III)) from photocurrent model of the ethanol-sensitized electrode. Reproduced with permission from Ref. [73]. Copyright 2014 American Chemical Society.

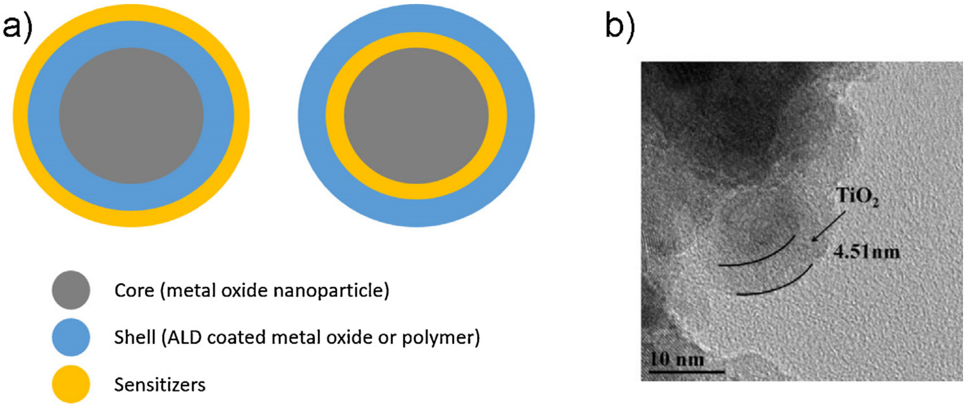

Fig. 9. (a) Cartoon depicting two types of core–shell architecture. (b) TEM image of a core–shell structure made from 75 ALD cycles of TiO_2 grown onto a SnO_2 film on FTO glass. Reproduced from Ref. [62].

found for the photoanode with the ALD Al_2O_3 coating, which, however, may not suggest higher Faradaic efficiency of oxygen generation, because a previous report [60] showed in a generator-collector experiment that TiO_2/RuP1 photoanodes with ALD Al_2O_3 overlayers did not produce O_2 despite their measurable photocurrent.

Dip-coating of dye-sensitized photoanodes with poly(methyl methacrylate) (PMMA) has also been studied as a way of stabilizing sensitizer dyes [67,98,99]. Unlike the vapor-phase ALD process, a PMMA coating can be applied by simply soaking the sensitized electrode in PMMA solution for a few seconds and drying in air (Fig. 14). Conformal PMMA coating throughout the oxide films was confirmed by TEM and FIB (focused ion beam)-SEM images [96], and the coating thickness could be controlled by varying the soaking time and PMMA concentration. Improved photocurrent stability was observed for samples coated with PMMA (Fig. 14). TAS of PMMA coated TiO_2-RuP1 at different pH values showed that back electron transfer rates were similar to electrodes without the PMMA treatment, and were independent of pH and PMMA thickness. This is in sharp contrast to ALD coating, in which the

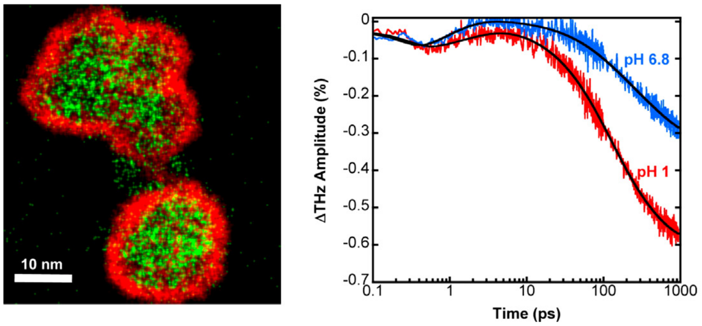

Fig. 10. (Left) High resolution energy dispersive X-ray spectroscopy mapping of a SnO_2/TiO_2 core–shell structure. Ti: red, Sn: green. (Center) TRTS measurement of a RuP1-sensitized SnO_2/TiO_2 photoanode in 0.1 M $HClO_4$ (pH 1, red) and 100 mM potassium phosphate buffer (pH 6.8, blue). (Right) Early picosecond kinetics of a RuP1-sensitized SnO_2/TiO_2 photoanode showing rapid recombination in the TiO_2 shell. Reproduced with permission from Ref. [88]. Copyright 2016 American Chemical Society. (For interpretation of the references to color in this figure legend, the reader is referred to the web version of the article.)

thickness has a dramatic influence on the electron recombination dynamics as discussed above. Photostability, determined by monitoring absorption spectra of the photoanode during illumination, was found to be enhanced, especially with thicker PMMA coatings. TiO_2-RuP1 treated with a 3.0 wt% PMMA solution, for example, retained 90% and 75% of its initial absorption after a 16 h soaking in pH 12 buffer solution in the dark and under illumination, respectively. Without the PMMA treatment, the electrodes were bleached completely during the test [98]. However, reduced photocurrent and cyclic voltammetry current from sensitized electrodes with thicker PMMA coatings implied that the insulating coating inhibited electron transfer between the electrode and the electrolyte [98,99]. In addition, with the PMMA coating, the electrolyte may not have access to all the pores of the mesoporous oxide films, because thicker PMMA coatings block the pores and the PMMA-coated surfaces are hydrophobic [98]. Ding et al. [67] immobilized molecular catalysts in the PMMA layer by mixing the PMMA solution with Ru5 molecules before coating a TiO_2-RuP1 photoanode with the mixture. The incorporation of catalyst molecules turned the PMMA coating into an active layer for water oxidation, and higher photocurrent was measured. However, the embedded catalyst molecules may prevent the formation of a conformal PMMA coating and the long-term stability of electrodes made by this technique remains to be explored.

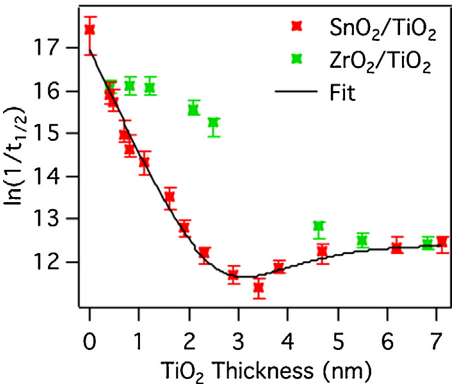

Fig. 11. Plot of $\ln(1/\tau_{1/2})$ vs. TiO_2 shell thickness for amorphous SnO_2/TiO_2 (red) and ZrO_2/TiO_2 (green) core–shell photoanodes at equal injection yields. $\tau_{1/2}$ is the time for half the total absorbance change in TAS measurement. The fit models the back electron transfer dynamics with contributions from both tunneling and localized shell recombination. Reproduced with permission from Ref. [84]. Copyright 2015 American Chemical Society. (For interpretation of the references to color in this figure legend, the reader is referred to the web version of the article.)

Photocathodes for water splitting dye cells

General principles

Water-splitting cells based on dye-sensitized photoanodes (Fig. 2) require a small bias voltage in order to function because electrons in TiO_2, SnO_2, ITO, and other typical oxide semiconductors are not sufficiently reducing to generate hydrogen from water. In principle, a tandem system that substitutes a photocathode for the dark catalytic cathode in Fig. 2 could split water without an applied bias. The study of such photocathodes has begun recently and is at a less advanced stage of development than the water-splitting photoanode. So far, several different photocathode architectures have been reported by different groups (Table 2). Most of these adapt the structure of *p*-type dye-sensitized solar cells (*p*-DSSC), in which wide bandgap *p*-type semiconductor nanoparticles (such as NiO) are deposited as a mesoporous thin film on a transparent conductive substrate for hole transport; molecular dyes adsorbed onto the nanoparticle surface serve as sensitizers for light absorption and excited charge carrier generation. Unlike the *p*-DSSC, in which a redox shuttle such as iodine/triiodide is used [100], the water-splitting photocathode requires the incorporation of a hydrogen-evolution reaction (HER) catalyst due to the slow kinetics of proton reduction. A schematic drawing of a dye-sensitized photocathode and the energy level alignment of each component are shown in Fig. 15. The efficiencies of electron transfer and charge collection depend on the energetic arrangement of the individual components. The valence band maximum (VBM) of the semiconductor needs to fall between the HOMO and LUMO of the sensitizer, and the conduction band maximum should be negative of the LUMO

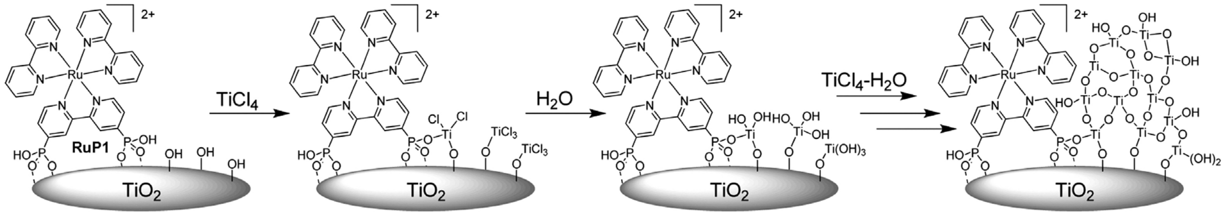

Fig. 12. Illustrative reaction scheme for ALD of $TiCl_4$-H_2O on TiO_2-RuP1. Adapted with permission from Ref. [91]. Copyright 2013 American Chemical Society.

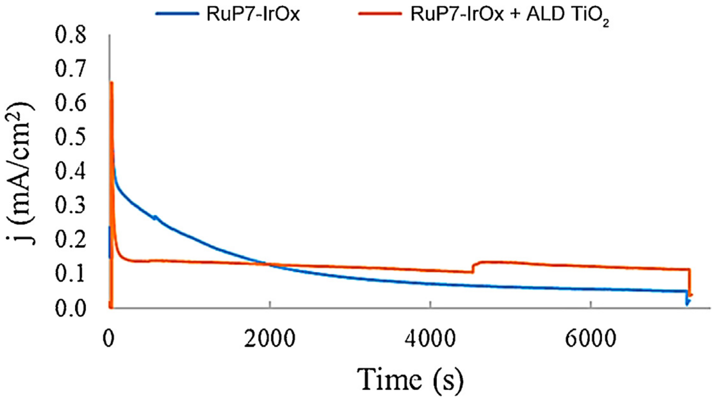

Fig. 13. Chronoamperometry of RuP7-IrO_x nanoparticle-sensitized *nano*ITO/TiO_2 photoanodes with and without an ALD TiO_2 coating in pH 5.8 buffer solution (Na_2SiF_6-$NaHCO_3$) at an applied bias of 300 mV vs. Ag/AgCl, illuminated at 455 nm and 14.5 mW/cm^2. Reproduced with permission from Ref. [65]. Copyright 2015 American Chemical Society.

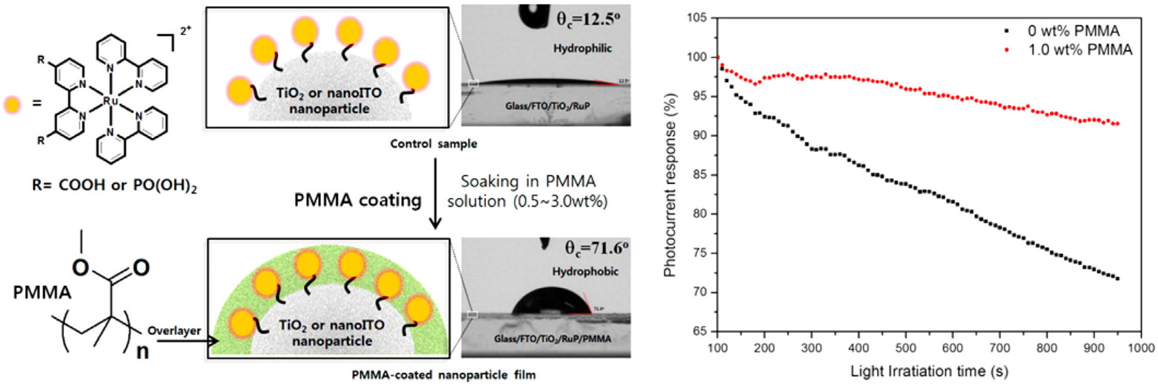

Fig. 14. Left: Schematic depictions of an added PMMA coating on a metal-oxide surface (TiO_2 or *nano*ITO) and the results of contact angle measurements on a mesoporous TiO_2 film before and after soaking in a PMMA/DCM coating solution. Right: Photocurrent stability comparison for TiO_2-RuP1 electrodes with and without a PMMA overlayer, tested in 0.1 M phosphate buffer, pH 7, with 0.4 M $NaClO_4$ and 20 mM hydroquinone as a sacrificial electron donor. Reproduced with permission from Ref. [98]. Copyright 2014 American Chemical Society.

Table 2
Photocathode sensitizers and assemblies for water-splitting dye cells.

Reference	Semiconductor	Dye	HER catalyst	Steady-state photocurrent (μA/cm^2)	Faradaic efficiency of H_2 generation	Photocurrent stability (h)	IPCE (wavelength)	Photocurrent test conditions
[104]	NiO	PMI-6T-TPA	n/a	1.7–3.9 (0.62 V)	97 ± 7%	4	ca. 0.4% (400 nm)	Xe lamp (>420 nm), pH 7
[105]	NiO	P1	Co1	5–18 (0.22 V)	n/a	0.5	n/a	Light emitting diode array (25 mW/cm2, >400 nm), pH 7
[106]	NiO	RuC2-Co1		8 (0.51 V)	68%	2.5	ca. 1.1% (400 nm)	Xe lamp (>420 nm) with water filter, pH 7
[107]	NiO	RuP1	Co2	13 (0.21 V)	n/a	n/a	n/a	Xe lamp (300 mW/cm^2, >400 nm) with water filter, pH 7
[63]	NiO	P1	Co3	20 (0.42 V)	68%	1.5	n/a	White LED light (100 mW/cm^2, >400 nm), pH7
[108]	n/a	Py-Ru	MoS_x nanoparticles	15 (0.33 V)	98%	4.17	n/a	Xe lamp (400–700 nm), pH 0.3
[109]	NiO	BH4	$Mo_3S_4^{4+}$ cluster	183 ± 36 (0 V)	49 ± 11%	16.6	1.54 ± 0.20% (460 nm)	Xe lamp (344 mW/cm^2, >420 nm), pH 0
[110]	NiO	DAT	Ni1	n/a	n/a	n/a	n/a	Xe-Hg lamp (>470 nm) with water filter, pH 2.1
[111]	NiO	RuP4	Ni3	4–8 (0.3 V)	8.6 ± 2.3%	2	n/a	Xe lamp (100 mW/cm^2, >400 nm) with water filter, pH 3
[112]	NiO	PMI	Co1 and Ni2	15 for Ni2, 25 for Co1 (−0.4 V vs. Ag/AgCl)	98 ± 4% for Ni2, 80 ± 10% for Co1	2	n/a	White LED light (100 mW/cm^2, >410 nm), 0.1 M H_2SO_4, 0.1 M Na_2SO_4 in 1:1 H_2O:MeCN
[113]	NiO	TPA-Co4		6–15 (0.14 V)	9.30%	3	n/a	Xe lamp (65 mW/cm^2, 400–800 nm), pH 5.5
[102]	NiO	C343	Fe1	10 (0.18 V)	50%	0.67	n/a	White LED light (mW/cm^2), pH 4.5

See Figs. 4 and 16 for structure codes.
Other notes for Table 1 also apply here.

of the sensitizer. The HER catalyst (E_{cat}) must be energetically capable of accepting an electron from the LUMO of the dye. This energetic arrangement promotes directional electron flow toward the HER catalyst. Excitons, produced by the sensitizer upon light excitation, dissociate at the dye-semiconductor interface and are reductively quenched by NiO within 1 ps [101–103]. An electron is then transferred from the reduced sensitizer to the HER catalyst, where proton reduction occurs. Typically the measured photocurrents and incident photon-to-current efficiencies (IPCE) of these photocathodes are very low, as they are compromised by several factors. The primary issues are poor hole injection, slow hole transport in the semiconductor, slow catalytic rates of proton reduction, and fast charge carrier recombination.

p-*Type semiconductors for water splitting photocathodes*

As shown in Table 2, NiO has so far been the only semiconductor used successfully as the hole transporting material in water-splitting photocathodes. NiO is a p-type semiconductor due to its mixed valence Ni^{2+} and Ni^{3+} states [114], and has an indirect band gap of 3.47 eV [115]. The flat-band potential of NiO, as an indication of the upper limit (in energy) of its valence band, is 0.47 V vs. NHE at pH 7 as measured by photocurrent onset potential [115]. A somewhat more positive value (0.53 V vs. NHE) has been measured by the Mott-Schottky method [116]. This relatively negative flat band potential is favorable for electron transfer from the semiconductor to photoexcited sensitizer molecules, making NiO a good candidate as a hole quencher. Like other oxide semiconductors, NiO exhibits a pH-dependent (ca. −60 mV/pH) flat-band potential shift in aqueous solutions because of protonation/deprotonation equilibria at the semiconductor-electrolyte interface. This implies that the driving force for reductive quenching of excited sensitizer molecules will be lower in acidic media [117].

Mesoporous NiO electrodes can be prepared via various routes, including electrodeposition [118], hydrothermal synthesis [119,120], sol-gel deposition [121,122], and block copolymer templating [123,124]. Wood et al. [125] compared the photoelectrochemical properties of dye-sensitized photocathodes made from different NiO sources (commercial and lab-made) as well as different deposition techniques (screen printed and doctor bladed) while using the same sensitizer and catalyst (P1 and Co1 in Fig. 16). Despite the use of different NiO sources and electrode assembly techniques, the photocurrents of all electrodes were similar in magnitude (ca. 10 $\mu A/cm^2$), and differences in current varied consistently with the specific surface area of the electrode, suggesting that NiO electrodes made under different conditions should possess comparable photoelectrochemical performance.

Compared to the *n*-type metal oxides used in DSSCs and water-splitting anodes, *p*-type metal oxide semiconductors typically have low charge carrier mobility. For example, the hole diffusion coefficient of mesoporous NiO in *p*-DSSCs is reported to be 10^{-8} to 10^{-7} cm^2/s, which is at least two orders of magnitude lower than the electron diffusion coefficient of TiO_2 used in *n*-DSSCs [126,127]. Poor hole transport kinetics lead to fast charge recombination, lowering the photoelectrochemical performance of the cell. The fact that charge recombination is the dominant kinetic pathway at both the photocathode and photoanode of water-splitting dye cells underscores the importance of controlling the architecture of the dye-semiconductor interface [128]. Surface quality plays an important role in charge separation and recombination, especially for nanomaterials with a high surface-to-volume ratio. Surface defects, which are often formed during preparation of the film (and are only partially removed by annealing), usually consist of atomic vacancies and dangling bonds. These can serve as trap sites for charge carriers, resulting in low charge separation yields. Kaeffer et al. [113] compared the XPS spectra of their photocathodes before and after 2-h photolysis. They found a change in the Ni^{3+}/Ni^{2+} ratio and the formation of metallic nickel, which indicated competitive reduction of bulk NiO during water reduction. Strategies for surface passivation and reducing the density of surface defects have been developed in recent years, such as increasing the crystallinity [129,130] and adding overlayers via ALD or solution-phase deposition [90,131,132]. ALD alumina in particular has been shown to be effective for enhancing the photocurrent of water-splitting photocathodes [106,113].

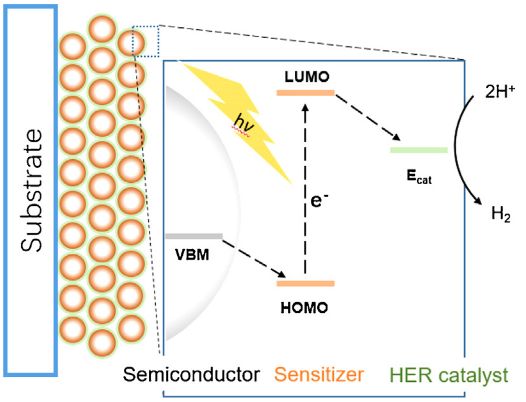

Fig. 15. Structure and energy scheme of the dye-sensitized photocathode for water splitting.

Considerations of ion balance in water-splitting solar cells suggest that the photocathode (photoanode) should be operated in strong acid (base), with two electrodes separated by a bipolar membrane [23,133]. This configuration can avoid the formation of a pH gradient across the membrane, which shifts the water redox potentials during continuous operation. Additionally, there is a greater driving force for proton reduction at lower cathode pH. From this perspective, NiO is not a good candidate as the hole-transport layer in water-splitting devices due to its solubility in acid. Surprisingly, Click et al. [109] recently reported an acid-stable water-splitting dye cell based on mesoporous NiO (Fig. 17, left). The cell was capable of 16.6 h continuous operation at pH 0. The acid stability of NiO in their experiments was achieved by using the sensitizer BH4, which was constructed based on the PMI-6T-TPA dye with one additional π-linker and acceptor unit. The hydrophobic hexyl group from the linker protects NiO against acid dissolution in aqueous electrolytes. The protection mechanism was demonstrated by the high contact angle of the electrode after dye sensitization and by a photocurrent onset potential of 400 mV vs NHE at pH 0. Working at this more favorable water reduction potential, this photocathode assembly produced a photocurrent as high as 254 $\mu A/cm^2$ (−0.2 V vs. NHE).

Photocathode sensitizers

The sensitizers listed in Table 2 are inherited from *p*-DSSCs, since extensive research on DSSCs has prepared a gallery of sensitizers for potential use in water-splitting cells [134,135]. The primary function of dye molecules is similar to that in the water splitting photoanode, namely light absorption, charge carrier injection, and charge transfer to an appropriate catalyst molecule or nanoparticle. At the photocathode, the basic requirements for sensitizers include: (1) strong absorption of visible light to maximize the utilization of solar energy, (2) a LUMO that is sufficiently negative of the water reduction couple, and a HOMO level that is more positive than the Fermi level of the semiconductor, (3) a long-lived charge-separated state for competitive photo-induced charge injection relative to recombination processes, and (4) stable attach-

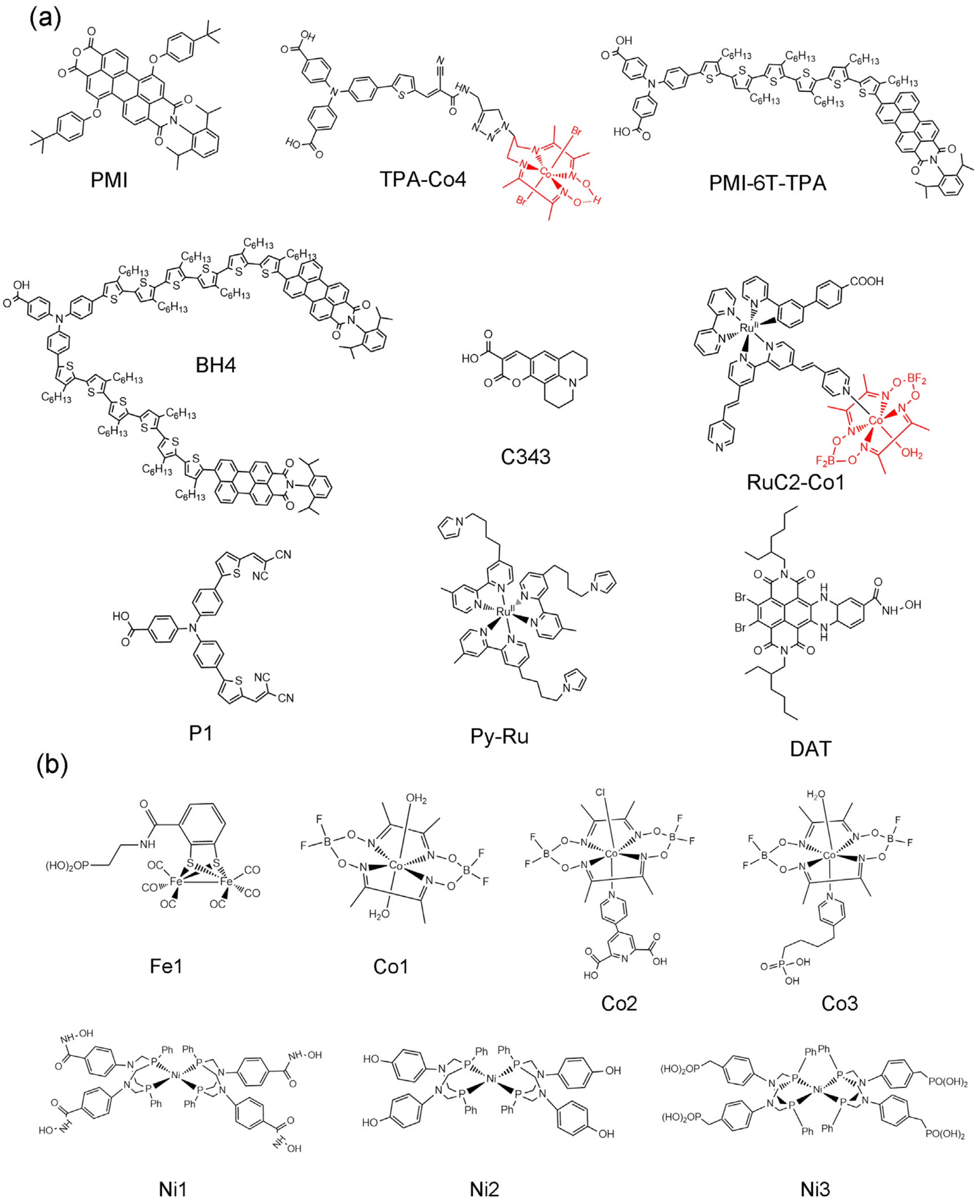

Fig. 16. Structures of the sensitizers (a) and catalysts (b) from the photocathodes summarized in Table 2 (catalyst is colored red when covalently connected to a sensitizer). (For interpretation of the references to color in this figure legend, the reader is referred to the web version of the article.)

ment to the semiconductor surface for efficient electron transfer and long-term stability.

While many naturally occurring dye molecules have been discovered that have strong visible absorption (1) and appropriate energetics (2), they generally suffer from fast relaxation of excited states (on the ps timescale) [136]. A great deal of research has focused on developing dyes with longer-lived excited and charge-separated states (3) for highly efficient DSSCs. Ruthenium polypyridyl sensitizers are widely used in DSSCs [134,135] because of their intense metal-to-ligand charge transfer (MLCT) absorption (extinction coefficient $\varepsilon_{452} = 14{,}600\,\mathrm{M}^{-1}\,\mathrm{cm}^{-1}$) [137] and long-lived ^{3}MLCT state (hundreds of ns) [138,139]. Their MLCT energies can be tuned by proper design of the substituents [128]. Among metal-free sensitizers, P1 in Fig. 16a exploits an electron push-pull mechanism, first proposed by Qin et al. [122], to extend the lifetime of its excited state. With a carboxylic acid-derivatized triarylamine core as the pusher and an electron-accepting unit, malononitrile, as the pulling group, the HOMO and LUMO can be spatially separated. Additional work has been done using donor-acceptor and donor-π-acceptor systems (PMI-6T-TPA and BH4), another strategy for long-lived charge-separation. In this mechanism, the chromophore is grafted through covalent bonding (conjugated π-linker group) to an electron donor or acceptor unit. Both mechanisms rely on the fact that the spatial separation of the sensitizer HOMO and LUMO can influence the lifetime of the excited state [140]. Several new diketopyrrolopyrrole (DPP) sensitizers for *p*-DSSCs, recently developed by Farre et al. [141], are promising for increasing the photocathode efficiency. It has been reported that hole injection

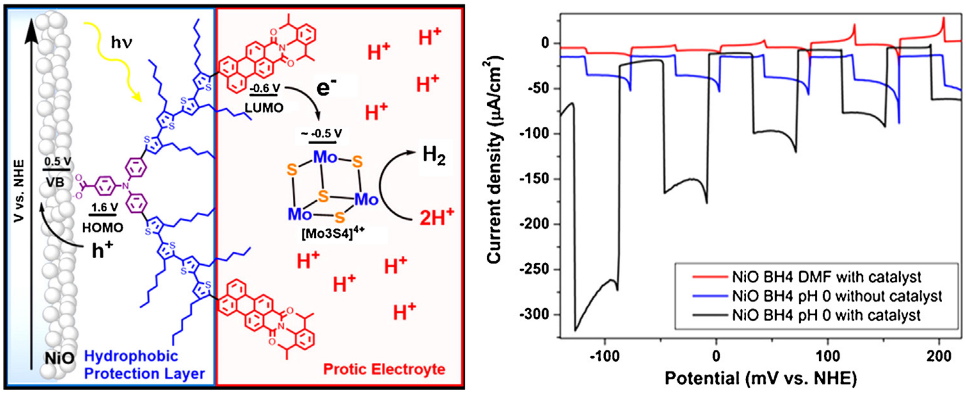

Fig. 17. Left: BH4-sensitized NiO photocathode and Mo-based HER catalyst with the energetics of hole and electron transfer. Right: linear voltammetric sweep with light chopping of a BH4-sensitized NiO electrode with varying electrolyte compositions. Reproduced with permission from Ref. [109]. Copyright 2016 American Chemical Society.

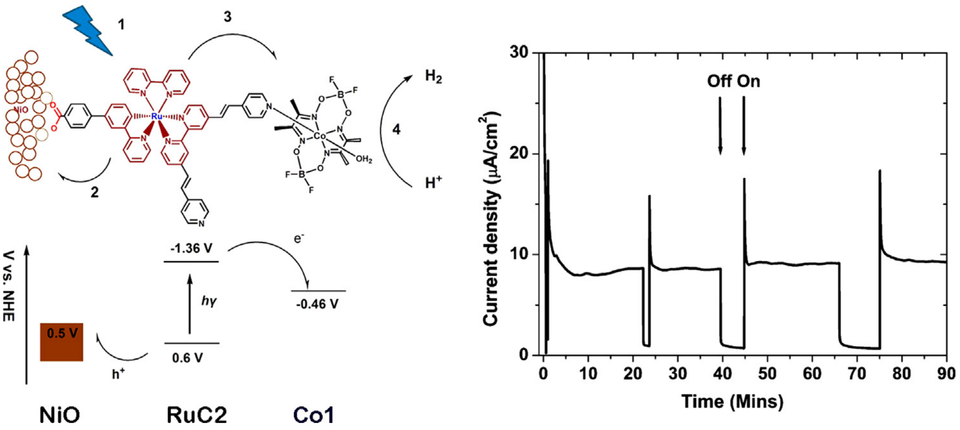

Fig. 18. Schematic drawing and energy level diagram (left) of the photocathode reported by Li et al. [106], and its corresponding chronoamperogram (right) under illumination at an applied bias of 0.1 V versus NHE. Reproduced with permission. Copyright 2013 American Chemical Society.

into NiO occurs within 10 ps. When the sensitizer is grafted to an electron acceptor, naphtalenediimide (NDI), the DPP-NDI assembly exhibits a long-lived charge separated state in $LiClO_4$/propylene carbonate solution, with an average lifetime of about 0.25 ms, up to 7 orders of magnitude longer than the timescale of hole injection.

Although anchoring groups (phosphonate and carboxylate, for example) are used to attach dye molecules onto the NiO surface, dye desorption still occurs under catalytic conditions. Using the "mummy" approach described above for dye-sensitized photoanodes, Kamire et al. [112] applied an ALD coating of Al_2O_3 to a PMI-sensitized NiO photocathode, which effectively prevented dye degradation and desorption at very negative potentials. The ALD Al_2O_3 coating also served to disaggregate the sensitizer molecules, as evidenced by the loss of excimer bands in steady-state and time-resolved spectra. When co-grafting sensitizers with chenodeoxycholic acid (CDCA), a classical coadsorbent that is used in dye-sensitized solar cells (DSSCs) to inhibit dye aggregation, Kaeffer et al. [113] also found improved stability of their photocathodes without loss of photocurrent.

Photocathode catalysts

Molecular HER catalysts, which are known for their high activity and tunability, have generally been used with dye-sensitized photocathodes. In the NiO-based photocathode reported by Tong et al. [104], the low photocurrent may be attributed to the lack of a HER catalyst despite the high Faradaic efficiency of H_2 generation. Cobaloxime, a class of highly active HER catalysts [142,143], has been used in several reports of water-splitting photocathodes (Table 2). In the first of these [105], Li et al. used the drop-casting method to add Co1 to a P1-sensitized NiO electrode, which resulted in rapid photocurrent decay due to the desorption of Co1. The same group later designed a co-sensitization approach to anchor both the molecular sensitizer (P1) and catalyst (Co1) directly onto NiO, achieving improved stability [63]. Ji et al. [106] improved the stability of this NiO-sensitizer-Co1 assembly by coordinating a Ru-based sensitizer directly to the cobalt metal center (Fig. 18). Stable photocurrent was observed for 2.5 h under illumination. More examples of chromophore-cobaloxime supramolecular assemblies are summarized in a recent review by Mulfort et al. [144]. Braumüller et al. [145] recently reported another supramolecular sensitizer-catalyst assembly in which the light-harvesting rutheniumpolypyridyl unit was connected to a Pt-based catalyst through a tetrapyridophenazine bridging ligand. This molecule was successfully immobilized onto a NiO surface, but the photoelectrochemical properties of the electrode have not yet been reported.

Using a RuP1/NiO photocathode, Castillo et al. [117] studied photo-excited electron transfer in acetonitrile between sensitizers and molecular HER catalysts based on Rh and Co complexes. They attributed the large photocurrent with Rh complexes to be the irreversible $Rh^{III/I}$ reduction process which resulted in slow back-electron transfer. Co complexes did not exhibit any photocurrent under the same experimental conditions because fast back-electron transfer from reduced catalyst molecules to NiO competes with electron transfer from RuP1 to Co^{II}. In this regard, the Rh catalysts may be more favorable for minimizing interfacial electron-hole combination in water-splitting photocathodes.

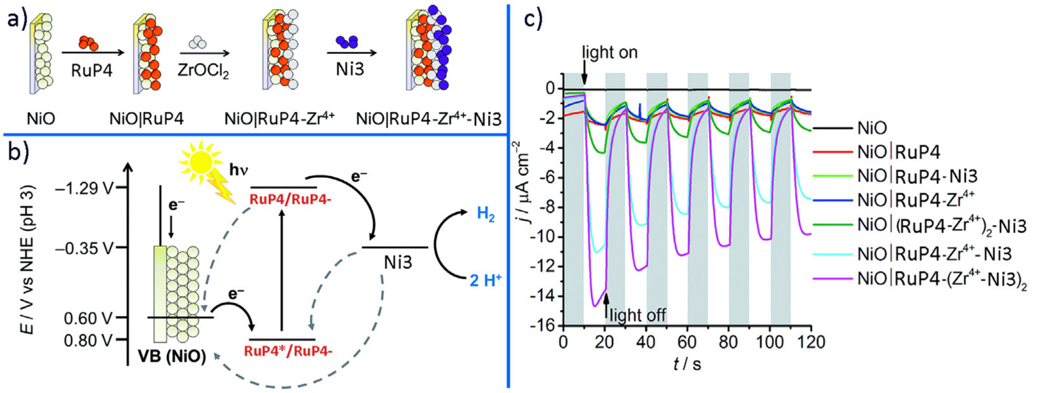

Fig. 19. (a) Supramolecular dye-catalyst assembly on a photocathode: layer-by-layer deposition of RuP4, Zr^{4+} and Ni3. (b) Energy level diagram of the supramolecular dye-catalyst assembly showing the electron transfer scheme. (c) Chronoamperometry of the assembled photocathode under chopped light irradiation at E_{appl} = 0.3 V vs. RHE. Reproduced from Ref. [111]. Published by The Royal Society of Chemistry.

Although the Co1 catalyst demonstrates efficient hydrogen evolution catalysis, its hydrolysis in acid limits its use under low pH conditions [109,146]. In the three recent studies of dye-sensitized photocathodes operating in acid, Lattach et al. [108] used MoS_x nanoparticles as the HER catalyst. The particles were electrodeposited into the Ru complex film prepared by electropolymerization of Py-Ru sensitizers onto a carbon electrode. Using BH4 dye to introduce a hydrophobic layer on the NiO surface, Click et al. [109] used a homogenous $[Mo_3S_4]^{4-}$ catalyst in acidic solution. In both reports, the performance of the photocathode improved significantly at lower pH. Van den Bosch et al. [110] recently reported a NiO-based photocathode using a co-immobilization strategy for grafting a Ni-DuBois-type HER catalyst, which is highly active for water reduction across a broad pH range [147]. However, neither photocurrent nor hydrogen was detected for the full dye/NiO/catalyst assembly, although the simple dye/NiO system was photoactive. The authors suggested that dye (or catalyst) aggregation and fast recombination from the reduced catalyst to oxidized NiO occur.

Gross et al. [111] simplified the connection of sensitizers to molecular HER catalysts by using Zr^{4+} cations for supramolecular assembly, using the layer-by-layer assembly method previously developed for dielectric and electron donor-acceptor assemblies [148,149] as well as chromophore-catalyst assemblies [54,150]. By adjusting the deposition cycles they were able to optimize the sensitizer/catalyst ratio for improved photocathode performance (Fig. 19).

Conclusions

Water-splitting in dye-sensitized solar cells, first demonstrated in 2009, still faces significant challenges in terms of its development as a useful route to solar fuel production. While much progress has been made on understanding the kinetics and mechanism of interfacial charge separation and recombination, the efficiency of both the photoanode and the photocathode remains low. The stability of molecular components, especially at the highly oxidizing potential of the photoanode, is also a problem in all systems studied to date. Nevertheless, research directed toward the charge separation and stability problems has produced clever approaches to both. The highest-performing molecular photoanodes now generate photocurrents for water oxidation in the range of several mA/cm^2, rivaling the best inorganic oxide photoanodes, and new designs of supramolecular sensitizers, molecular catalysts, and core–shell electrodes have significantly impacted both the efficiency and stability of photoanodes and photocathodes. The modular nature of the system, and the vast tunability accessible in the molecular space, offer many degrees of freedom for re-designing the architecture, and for incorporating new light absorbers, catalysts, and protection strategies as they are developed.

Acknowledgments

This work was supported by the Office of Basic Energy Sciences, Division of Chemical Sciences, Geosciences, and Energy Biosciences, Department of Energy, under contracts DE-FG02-07ER15911. N.S.M. thanks the National Science Foundation for support as a graduate fellow under Grant DGE1255832.

References

[1] D. Feldman, G. Barbose, R. Margolis, M. Bolinger, D. Chung, R. Fu, J. Seel, C. Davidson, R. Wiser, Photovoltaic System Pricing Trends: Historical, Recent, and Near-Term Projections, 2015, NREL/PR-6A20-64898.
[2] Monthly Energy Review, December 2016, U.S. Energy Information Administration, DOE/EIA-0035(2016/12).
[3] J.H. Williams, A. Debenedictis, R. Ghanadan, A. Mahone, J. Moore, W.R.M. Iii, S. Price, M.S. Torn, Science 335 (2012) 53–60.
[4] M.Z. Jacobson, M.A. Delucchi, M.A. Cameron, B.A. Frew, Proc. Natl. Acad. Sci. U.S.A. 112 (2015) 15060–15065.
[5] S.H. Jensen, C. Graves, M. Mogensen, C. Wendel, R. Braun, G. Hughes, Z. Gao, S.A. Barnett, Energy Environ. Sci. 8 (2015) 2471–2479.
[6] E.E. Barton, D.M. Rampulla, A.B. Bocarsly, J. Am. Chem. Soc. 130 (2008) 6342–6344.
[7] A.J. Morris, G.J. Meyer, E. Fujita, Acc. Chem. Res. 42 (2009) 1983–1994.
[8] G.K. Ramesha, J.F. Brennecke, P.V. Kamat, ACS Catal. 4 (2014) 3249–3254.
[9] M.S. Hamdy, R. Amrollahi, I. Sinev, B. Mei, G. Mul, J. Am. Chem. Soc. 136 (2014) 594–597.
[10] F. Sastre, A.V. Puga, L. Liu, A. Corma, H. García, J. Am. Chem. Soc. 136 (2014) 6798–6801.
[11] M. Schreier, P. Gao, M.T. Mayer, J. Luo, T. Moehl, M.K. Nazeeruddin, S.D. Tilley, M. Grätzel, Energy Environ. Sci. 8 (2015) 855–861.
[12] F. Sastre, M. Oteri, A. Corma, H. García, Energy Environ. Sci. 6 (2013) 2211–2215.
[13] L.B. Hoch, T.E. Wood, P.G. O'Brien, K. Liao, L.M. Reyes, C.A. Mims, G.A. Ozin, Adv. Sci. 1 (2014) 1400013.
[14] H. Li, J. Shang, Z. Ai, L. Zhang, J. Am. Chem. Soc. 137 (2015) 6393–6399.
[15] A. Banerjee, B.D. Yuhas, E.A. Margulies, Y. Zhang, Y. Shim, M.R. Wasielewski, M.G. Kanatzidis, J. Am. Chem. Soc. 137 (2015) 2030–2034.
[16] A. Fujishima, K. Honda, Nature 238 (1972) 37–38.
[17] K. Maeda, K. Teramura, D. Lu, T. Takata, N. Saito, Y. Inoue, K. Domen, Nature 440 (2006) 295.
[18] J.H. Alstrum-Acevedo, M.K. Brennaman, T.J. Meyer, Inorg. Chem. 44 (2005) 6802–6827.
[19] R.E. Blankenship, D.M. Tiede, J. Barber, G.W. Brudvig, G. Fleming, M. Ghirardi, M.R. Gunner, W. Junge, D.M. Kramer, A. Melis, T. Moore, C.C. Moser, D.G. Nocera, A.J. Nozik, D.R. Ort, W.W. Parson, R.C. Prince, R.T. Sayre, Science 332 (2011) 805–809.
[20] S. Rühle, Sol. Energy 130 (2016) 139–147.
[21] J.R. Bolton, S.J. Strickler, J.S. Connolly, Nature 316 (1985) 495–500.
[22] J.R. Bolton, Sol. Energy 57 (1996) 37–50.
[23] E.A. Hernández-Pagán, N.M. Vargas-Barbosa, T. Wang, Y. Zhao, E.S. Smotkin, T.E. Mallouk, Energy Environ. Sci. 5 (2012) 7582–7589.

[24] M.R. Singh, K. Papadantonakis, C. Xiang, N.S. Lewis, Energy Environ. Sci. 8 (2015) 2760–2767.
[25] O. Khaselev, J.A. Turner, Science 280 (1998) 425–427.
[26] S. Licht, B. Wang, S. Mukerji, T. Soga, M. Umeno, H. Tributsch, Int. J. Hydrogen Energy 26 (2001) 653–659.
[27] S.Y. Reece, J.A. Hamel, K. Sung, T.D. Jarvi, A.J. Esswein, J.J.H. Pijpers, D.G. Nocera, Science 334 (2011) 645–648.
[28] J. Luo, D.A. Vermaas, D. Bi, A. Hagfeldt, W.A. Smith, M. Grätzel, Adv. Energy Mater. 6 (2016) 1600100.
[29] B.A. Pinaud, J.D. Benck, L.C. Seitz, A.J. Forman, Z. Chen, T.G. Deutsch, B.D. James, K.N. Baum, G.N. Baum, S. Ardo, H. Wang, E. Miller, T.F. Jaramillo, Energy Environ. Sci. 6 (2013) 1983–2002.
[30] N.S. Lewis, Science 351 (2016) 353.
[31] F.E. Osterloh, Chem. Soc. Rev. 42 (2013) 2294–2320.
[32] N. Vlachopoulos, P. Liska, J. Augustynski, M. Grätzel, J. Am. Chem. Soc. 110 (1988) 1216–1220.
[33] B. O'Regan, M. Grätzel, Nature 353 (1991) 737–740.
[34] S. Mathew, A. Yella, P. Gao, R. Humphry-Baker, B.F.E. Curchod, N. Ashari-Astani, I. Tavernelli, U. Rothlisberger, M.K. Nazeeruddin, M. Grätzel, Nat. Chem 6 (2014) 242–247.
[35] J.W. Youngblood, S.H.A. Lee, Y. Kobayashi, E.A. Hernandez-Pagan, P.G. Hoertz, T.A. Moore, A.L. Moore, D. Gust, T.E. Mallouk, J. Am. Chem. Soc. 131 (2009) 926–927.
[36] A. Kudo, Y. Miseki, Chem. Soc. Rev. 38 (2009) 253–278.
[37] A. Kay, I. Cesar, M. Grätzel, J. Am. Chem. Soc. 128 (2006) 15714–15721.
[38] R. van de Krol, Y. Liang, J. Schoonman, J. Mater. Chem. 18 (2008) 2311–2320.
[39] T.W. Kim, K.-S. Choi, Science 343 (2014) 990–994.
[40] T.W. Kim, Y. Ping, G.A. Galli, K.-S. Choi, Nat. Commun. 6 (2015) 8769.
[41] J.G. Rowley, B.H. Farnum, S. Ardo, G.J. Meyer, J. Phys. Chem. Lett. 1 (2010) 3132–3140.
[42] R. Brimblecombe, A. Koo, G.C. Dismukes, G.F. Swiegers, L. Spiccia, J. Am. Chem. Soc. 132 (2010) 2892–2894.
[43] L. Li, L. Duan, Y. Xu, M. Gorlov, A. Hagfeldt, L. Sun, Chem. Commun. 46 (2010) 7307.
[44] G.F. Moore, J.D. Blakemore, R.L. Milot, J.F. Hull, H. Song, L. Cai, C.A. Schmuttenmaer, R.H. Crabtree, G.W. Brudvig, Energy Environ. Sci. 4 (2011) 2389–2392.
[45] M. Bledowski, L. Wang, A. Ramakrishnan, O.V. Khavryuchenko, V.D. Khavryuchenko, P.C. Ricci, J. Strunk, T. Cremer, C. Kolbeck, R. Beranek, Phys. Chem. Chem. Phys. 13 (2011) 21511–21519.
[46] M. Bledowski, L. Wang, A. Ramakrishnan, A. Bétard, O.V. Khavryuchenko, R. Beranek, ChemPhysChem 13 (2012) 3018–3024.
[47] S.A. Lee, Y. Zhao, E.A. Hernandez-Pagan, L. Blasdel, W.J. Youngblood, T.E. Mallouk, Faraday Discuss. 155 (2012) 165–176.
[48] Y. Zhao, J.R. Swierk, J.D. Megiatto, B. Sherman, W.J. Youngblood, D. Qin, D.M. Lentz, A.L. Moore, T.A. Moore, D. Gust, T.E. Mallouk, Proc. Natl. Acad. Sci. U.S.A. 109 (2012) 15612–15616.
[49] X. Xiang, J. Fielden, W. Rodríguez-Córdoba, Z. Huang, N. Zhang, Z. Luo, D.G. Musaev, T. Lian, C.L. Hill, J. Phys. Chem. C 117 (2013) 918–926.
[50] Y. Gao, X. Ding, J. Liu, L. Wang, Z. Lu, L. Li, L. Sun, J. Am. Chem. Soc. 135 (2013) 4219–4222.
[51] L. Alibabaei, M.K. Brennaman, M.R. Norris, B. Kalanyan, W. Song, M.D. Losego, J.J. Concepcion, R.A. Binstead, G.N. Parsons, T.J. Meyer, Proc. Natl. Acad. Sci. U.S.A. 110 (2013) 20008–20013.
[52] J.R. Swierk, N.S. McCool, T.P. Saunders, G.D. Barber, M.E. Strayer, N.M. Vargas-Barbosa, T.E. Mallouk, J. Phys. Chem. C 118 (2014) 17046–17053.
[53] Y. Gao, L. Zhang, X. Ding, L. Sun, Phys. Chem. Chem. Phys. 16 (2014) 12008–12013.
[54] X. Ding, Y. Gao, L. Zhang, Z. Yu, J. Liu, L. Sun, ACS Catal. 4 (2014) 2347–2350.
[55] J.T. Kirner, J.J. Stracke, B.A. Gregg, R.G. Finke, ACS Appl. Mater. Interfaces 6 (2014) 13367–13377.
[56] X. Ding, Y. Gao, L. Zhang, Z. Yu, J. Liu, L. Sun, Electrochim. Acta 149 (2014) 337–340.
[57] P.K. Poddutoori, J.M. Thomsen, R.L. Milot, S.W. Sheehan, C.F.A. Negre, V.K.R. Garapati, C.A. Schmuttenmaer, V.S. Batista, G.W. Brudvig, A. van der Est, J. Mater. Chem. A 3 (2015) 3868–3879.
[58] J. Fielden, J.M. Sumliner, N. Han, Y.V. Geletii, X. Xiang, D.G. Musaev, T. Lian, C.L. Hill, Chem. Sci. 6 (2015) 5531–5543.
[59] O.V. Khavryuchenko, L. Wang, D. Mitoraj, G.H. Peslherbe, R. Beranek, J. Coord. Chem. 68 (2015) 3317–3327.
[60] A.M. Lapides, B.D. Sherman, M.K. Brennaman, C.J. Dares, K.R. Skinner, J.L. Templeton, T.J. Meyer, Chem. Sci. 6 (2015) 6398–6406.
[61] J.R. Swierk, D.D. Méndez-Hernández, N.S. McCool, P. Liddell, Y. Terazono, I. Pahk, J.J. Tomlin, N.V. Oster, T.A. Moore, A.L. Moore, D. Gust, T.E. Mallouk, Proc. Natl. Acad. Sci. U.S.A. 112 (2015) 1681–1686.
[62] L. Alibabaei, B.D. Sherman, M.R. Norris, M.K. Brennaman, T.J. Meyer, Proc. Natl. Acad. Sci. U.S.A. 112 (2015) 5899–5902.
[63] F. Li, K. Fan, B. Xu, E. Gabrielsson, Q. Daniel, L. Li, L. Sun, J. Am. Chem. Soc. 137 (2015) 9153–9159.
[64] B.D. Sherman, D.L. Ashford, A.M. Lapides, M.V. Sheridan, K.-R. Wee, T.J. Meyer, J. Phys. Chem. Lett. 6 (2015) 3213–3217.
[65] K.E. Michaux, A.A. Gambardella, L. Alibabaei, D.L. Ashford, B.D. Sherman, R.A. Binstead, T.J. Meyer, R.W. Murray, J. Phys. Chem. C 119 (2015) 17023–17027.
[66] K.-R. Wee, B.D. Sherman, M.K. Brennaman, M.V. Sheridan, A. Nayak, L. Alibabaei, T.J. Meyer, J. Mater. Chem. A 4 (2016) 2969–2975.
[67] X. Ding, Y. Gao, L. Ye, L. Zhang, L. Sun, ChemSusChem 8 (2015) 3992–3995.
[68] M. Yamamoto, L. Wang, F. Li, T. Fukushima, K. Tanaka, L. Sun, H. Imahori, Chem. Sci. 7 (2016) 1430–1439.
[69] H. Li, F. Li, Y. Wang, L. Bai, F. Yu, L. Sun, Chempluschem 81 (2016) 1056–1059.
[70] G. Leem, B.D. Sherman, A.J. Burnett, Z.A. Morseth, K.-R. Wee, J.M. Papanikolas, T.J. Meyer, K.S. Schanze, ACS Energy Lett. 1 (2016) 339–343.
[71] B.D. Sherman, Y. Xie, M.V. Sheridan, D. Wang, D.W. Shaffer, T.J. Meyer, J.J. Concepcion, ACS Energy Lett. 2 (2016) 124–128.
[72] B.D. Sherman, M.V. Sheridan, K.-R. Wee, S.L. Marquard, D. Wang, L. Alibabaei, D.L. Ashford, T.J. Meyer, J. Am. Chem. Soc. 138 (2016) 16745–16753.
[73] J.R. Swierk, N.S. McCool, T.P. Saunders, G.D. Barber, T.E. Mallouk, J. Am. Chem. Soc. 136 (2014) 10974–10982.
[74] J.R. Swierk, N.S. McCool, T.E. Mallouk, J. Phys. Chem. C 119 (2015) 13858–13867.
[75] N.S. McCool, J.R. Swierk, C.T. Nemes, T.P. Saunders, C.A. Schmuttenmaer, T.E. Mallouk, ACS Appl. Mater. Interfaces 8 (2016) 16727–16735.
[76] J. Nelson, A.M. Eppler, I.M. Ballard, J. Photochem. Photobiol. A: Chem. 148 (2002) 25–31.
[77] K. Hanson, M.K. Brennaman, A. Ito, H. Luo, W. Song, K.A. Parker, R. Ghosh, M.R. Norris, C.R.K. Glasson, J.J. Concepcion, R. Lopez, T.J. Meyer, J. Phys. Chem. C 116 (2012) 14837–14847.
[78] A.F. Halverson, K. Zhu, P.T. Erslev, J.Y. Kim, N.R. Neale, A.J. Frank, Nano Lett. 12 (2012) 2112–2116.
[79] S.J. Fonash, Solar Cell Device Physics, 2nd ed., Elsevier Inc., 2010.
[80] S.G. Chen, S. Chappel, Y. Diamant, A. Zaban, Chem. Mater. 13 (2001) 4629–4634.
[81] A. Kay, M. Grätzel, Chem. Mater. 14 (2002) 2930–2935.
[82] E. Palomares, J.N. Clifford, S.A. Haque, T. Lutz, J.R. Durrant, J. Am. Chem. Soc. 125 (2003) 475–482.
[83] D.L. Ashford, M.K. Gish, A.K. Vannucci, M.K. Brennaman, J.L. Templeton, J.M. Papanikolas, T.J. Meyer, Chem. Rev. 115 (2015) 13006–13049.
[84] R.R. Knauf, B. Kalanyan, G.N. Parsons, J.L. Dempsey, J. Phys. Chem. C 119 (2015) 28353–28360.
[85] N.S. McCool, J.R. Swierk, C.T. Nemes, C.A. Schmuttenmaer, T.E. Mallouk, J. Phys. Chem. Lett. (2016) 2930–2934.
[86] M.K. Gish, A.M. Lapides, M.K. Brennaman, J.L. Templeton, T.J. Meyer, J.M. Papanikolas, J. Phys. Chem. Lett. (2016) 5297–5301.
[87] S.M. George, Chem. Rev. 110 (2010) 111–131.
[88] J.R. Swierk, N.S. McCool, C.T. Nemes, T.E. Mallouk, C.A. Schmuttenmaer, J. Phys. Chem. C 120 (2016) 5940–5948.
[89] C. Prasittichai, J.R. Avila, O.K. Farha, J.T. Hupp, J. Am. Chem. Soc. 135 (2013) 16328–16331.
[90] C.J. Flynn, S.M. McCullough, E. Oh, L. Li, C.C. Mercado, B.H. Farnum, W. Li, C.L. Donley, W. You, A.J. Nozik, J.R. McBride, T.J. Meyer, Y. Kanai, J.F. Cahoon, ACS Appl. Mater. Interfaces 8 (2016) 4754–4761.
[91] K. Hanson, M.D. Losego, B. Kalanyan, G.N. Parsons, T.J. Meyer, Nano Lett. 13 (2013) 4802–4809.
[92] K. Hanson, M.D. Losego, B. Kalanyan, D.L. Ashford, G.N. Parsons, T.J. Meyer, Chem. Mater. 25 (2013) 3–5.
[93] J.R. Swierk, K.P. Regan, J. Jiang, G.W. Brudvig, C.A. Schmuttenmaer, ACS Energy Lett. (2016) 603–606.
[94] H.-J. Son, X. Wang, C. Prasittichai, N.C. Jeong, T. Aaltonen, R.G. Gordon, J.T. Hupp, J. Am. Chem. Soc. 134 (2012) 9537–9540.
[95] H.-J. Son, C. Prasittichai, J.E. Mondloch, L. Luo, J. Wu, D.W. Kim, O.K. Farha, J.T. Hupp, J. Am. Chem. Soc. 135 (2013) 11529–11532.
[96] D.H. Kim, M.D. Losego, K. Hanson, L. Alibabaei, K. Lee, T.J. Meyer, G.N. Parsons, Phys. Chem. Chem. Phys. 16 (2014) 8615–8622.
[97] H.-J. Son, C.H. Kim, D.W. Kim, N.C. Jeong, C. Prasittichai, L. Luo, J. Wu, O.K. Farha, M.R. Wasielewski, J.T. Hupp, ACS Appl. Mater. Interfaces 7 (2015) 5150–5159.
[98] K.R. Wee, M.K. Brennaman, L. Alibabaei, B.H. Farnum, B. Sherman, A.M. Lapides, T.J. Meyer, J. Am. Chem. Soc. 136 (2014) 13514–13517.
[99] L. Zhang, Y. Gao, X. Ding, Electrochim. Acta 207 (2016) 130–134.
[100] F. Odobel, L. Le Pleux, Y. Pellegrin, E. Blart, Acc. Chem. Res. 43 (2010) 1063–1071.
[101] M. Brautigam, J. Kubel, M. Schulz, J.G. Vos, B. Dietzek, Phys. Chem. Chem. Phys. 17 (2015) 7823–7830.
[102] L.J. Antila, P. Ghamgosar, S. Maji, H. Tian, S. Ott, L. Hammarström, ACS Energy Lett. (2016) 1106–1111.
[103] A.M. Brown, L.J. Antila, M. Mirmohades, S. Pullen, S. Ott, L. Hammarström, J. Am. Chem. Soc. 138 (2016) 8060–8063.
[104] L. Tong, A. Iwase, A. Nattestad, U. Bach, M. Weidelener, G. Götz, A. Mishra, P. Bäuerle, R. Amal, G.G. Wallace, A.J. Mozer, Energy Environ. Sci. 5 (2012) 9472–9475.
[105] L. Li, L. Duan, F. Wen, C. Li, M. Wang, A. Hagfeldt, L. Sun, Chem. Commun. 48 (2012) 988–990.
[106] Z. Ji, M. He, Z. Huang, U. Ozkan, Y. Wu, J. Am. Chem. Soc. 135 (2013) 11696–11699.
[107] K. Fan, F. Li, L. Wang, Q. Daniel, E. Gabrielsson, L. Sun, Phys. Chem. Chem. Phys. 16 (2014) 25234–25240.
[108] Y. Lattach, J. Fortage, A. Deronzier, J.-C. Moutet, ACS Appl. Mater. Interfaces 7 (2015) 4476–4480.
[109] K.A. Click, D.R. Beauchamp, Z. Huang, W. Chen, Y. Wu, J. Am. Chem. Soc. 138 (2016) 1174–1179.
[110] B. van den Bosch, J.A. Rombouts, R.V.A. Orru, J.N.H. Reek, R.J. Detz, ChemCatChem 8 (2016) 1392–1398.

[111] M.A. Gross, C.E. Creissen, K.L. Orchard, E. Reisner, Chem. Sci. 6 (2016) 242–247.
[112] R.J. Kamire, M.B. Majewski, W.L. Hoffeditz, B.T. Phelan, O.K. Farha, J.T. Hupp, M.R. Wasielewski, Chem. Sci. 22 (2017) 32–57.
[113] N. Kaeffer, J. Massin, C. Lebrun, O. Renault, M. Chavarot-Kerlidou, V. Artero, J. Am. Chem. Soc. 138 (2016) 12308–12311.
[114] D.M. Tench, E. Yeager, J. Electrochem. Soc. 120 (1973) 164–171.
[115] F.P. Koffyberg, J. Electrochem. Soc. 128 (1981) 2476–2479.
[116] T.O. Rouse, J.L. Weininger, J. Electrochem. Soc. 113 (1966) 184–190.
[117] C.E. Castillo, M. Gennari, T. Stoll, J. Fortage, A. Deronzier, M.N. Collomb, M. Sandroni, F. Légalité, E. Blart, Y. Pellegrin, C. Delacote, M. Boujtita, F. Odobel, P. Rannou, S. Sadki, J. Phys. Chem. C 119 (2015) 5806–5818.
[118] F. Vera, R. Schrebler, E. Muñoz, C. Suarez, P. Cury, H. Gómez, R. Córdova, R.E. Marotti, E.A. Dalchiele, Thin Solid Films 490 (2005) 182–188.
[119] L. Lepleux, B. Chavillon, Y. Pellegrini, E. Blart, L. Cario, S. Jobic, F. Odobel, Inorg. Chem. 48 (2009) 8245–8250.
[120] D.-B. Kuang, B.-X. Lei, Y.-P. Pan, X.-Y. Yu, C.-Y. Su, J. Phys. Chem. C 113 (2009) 5508–5513.
[121] H. Zhu, A. Hagfeldt, G. Boschloo, J. Phys. Chem. C 111 (2007) 17455–17458.
[122] P. Qin, H. Zhu, T. Edvinsson, G. Boschloo, A. Hagfeldt, L. Sun, J. Am. Chem. Soc. 130 (2008) 8570–8571.
[123] L. Li, E.A. Gibson, P. Qin, G. Boschloo, M. Gorlov, A. Hagfeldt, L. Sun, Adv. Mater. 22 (2010) 1759–1762.
[124] S. Sumikura, S. Mori, S. Shimizu, H. Usami, E. Suzuki, J. Photochem. Photobiol. A: Chem. 199 (2008) 1–7.
[125] C.J. Wood, G.H. Summers, C.A. Clark, N. Kaeffer, M. Braeutigam, L.R. Carbone, L. D'Amario, K. Fan, Y. Farré, S. Narbey, F. Oswald, L.A. Stevens, C.D.J. Parmenter, M.W. Fay, A. La Torre, C.E. Snape, B. Dietzek, D. Dini, L. Hammarström, Y. Pellegrin, F. Odobel, L. Sun, V. Artero, E.A. Gibson, Phys. Chem. Chem. Phys. 18 (2016) 10727–10738.
[126] S. Mori, S. Fukuda, S. Sumikura, Y. Takeda, Y. Tamaki, E. Suzuki, T. Abe, J. Phys. Chem. C 112 (2008) 16134–16139.
[127] S. Nakade, T. Kanzaki, Y. Wada, S. Yanagida, Langmuir 21 (2005) 10803–10807.
[128] J.R. Swierk, T.E. Mallouk, Chem. Soc. Rev. 42 (2013) 2357–2387.
[129] X.L. Zhang, Z. Zhang, D. Chen, P. Bäuerle, U. Bach, Y.-B. Cheng, Chem. Commun. 48 (2012) 9885–9887.
[130] E.A. Gibson, M. Awais, D. Dini, D.P. Dowling, M.T. Pryce, J.G. Vos, G. Boschloo, A. Hagfeldt, Phys. Chem. Chem. Phys. 15 (2013) 2411–2420.
[131] S. Uehara, S. Sumikura, E. Suzuki, S. Mori, Energy Environ. Sci. 3 (2010) 641–644.
[132] G. Natu, Z. Huang, Z. Ji, Y. Wu, Langmuir 28 (2012) 950–956.
[133] N.M. Vargas-Barbosa, G.M. Geise, M.A. Hickner, T.E. Mallouk, ChemSusChem 7 (2014) 3017–3020.
[134] P. Chawla, M. Tripathi, Int. J. Energy Res. 39 (2015) 1579–1596.
[135] C.-P. Lee, R.Y.-Y. Lin, L.-Y. Lin, C.-T. Li, T.-C. Chu, S.-S. Sun, J.T. Lin, K.-C. Ho, RSC Adv. 5 (2015) 23810–23825.
[136] G. Calogero, A. Bartolotta, G. Di Marco, A. Di Carlo, F. Bonaccorso, Chem. Soc. Rev. 44 (2015) 3244–3294.
[137] K. Kalyanasundaram, Coord. Chem. Rev. 46 (1982) 159–244.
[138] S.W. Keller, S.A. Johnson, E.S. Brigham, E.H. Yonemoto, T.E. Mallouk, J. Am. Chem. Soc. 117 (1995) 12879–12880.
[139] D.M. Kaschak, J.T. Lean, C.C. Waraksa, G.B. Saupe, H. Usami, T.E. Mallouk, J. Am. Chem. Soc. 121 (1999) 3435–3445.
[140] F. Odobel, Y. Pellegrin, E.A. Gibson, A. Hagfeldt, A.L. Smeigh, L. Hammarström, Coord. Chem. Rev. 256 (2012) 2414–2423.
[141] Y. Farré, L. Zhang, Y. Pellegrin, A. Planchat, E. Blart, M. Boujtita, L. Hammarström, D. Jacquemin, F. Odobel, J. Phys. Chem. C 120 (2016) 7923–7940.
[142] C. Baffert, V. Artero, M. Fontecave, Inorg. Chem. 46 (2007) 1817–1824.
[143] J.L. Dempsey, B.S. Brunschwig, J.R. Winkler, H.B. Gray, Acc. Chem. Res. 42 (2009) 1995–2004.
[144] K.L. Mulfort, L.M. Utschig, Acc. Chem. Res. 49 (2016) 835–843.
[145] M. Braumüller, M. Schulz, D. Sorsche, M. Pfeffer, M. Schaub, J. Popp, B.-W. Park, A. Hagfeldt, B. Dietzek, S. Rau, Dalton Trans. 44 (2015) 5577–5586.
[146] P.-A. Jacques, V. Artero, J. Pécaut, M. Fontecave, Proc. Natl. Acad. Sci. U.S.A. 106 (2009) 20627–20632.
[147] A. Dutta, D.L. DuBois, J.A.S. Roberts, W.J. Shaw, Proc. Natl. Acad. Sci. U.S.A. 111 (2014) 16286–16291.
[148] H. Lee, L.J. Kepley, H.G. Hong, S. Akhter, T.E. Mallouk, J. Phys. Chem. 92 (1988) 2597–2601.
[149] T. Ishida, K. Terada, K. Hasegawa, H. Kuwahata, K. Kusama, R. Sato, M. Nakano, Y. Naitoh, M. Haga, Appl. Surf. Sci. 255 (2009) 8824–8830.
[150] K. Hanson, D.A. Torelli, A.K. Vannucci, M.K. Brennaman, H. Luo, L. Alibabaei, W. Song, D.L. Ashford, M.R. Norris, C.R.K. Glasson, J.J. Concepcion, T.J. Meyer, Angew. Chem. Int. Ed. 51 (2012) 12782–12785.

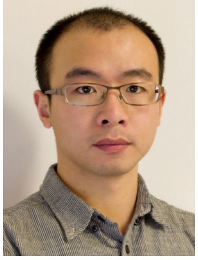

Pengtao Xu received his B.S. degree from Nankai University and is currently a Ph.D. student in Chemistry at Penn State, where he is a member of the Mallouk research group. His research interests include photoelectrochemistry and the chemistry of layered materials. He has contributed to both experimental and theoretical studies as a Ph.D. student, focusing on layered oxide and layered chalcogenide semiconductors, as well as on the cathode and anode of water-splitting dye-sensitized solar cells.

Nicholas McCool received his B.S. degree from Rutgers University, where he did undergraduate research with Prof. Charles Dismukes on oxygen evolution catalysis, and received his Ph.D. degree in Chemistry from Penn State. As a graduate student in the Mallouk group, he studied the mechanisms of charge separation and charge recombination in water-splitting dye-sensitized solar cells by using electrochemical and ultrafast spectroscopic techniques.

Thomas Mallouk received his BSc. from Brown University and his Ph.D. in Chemistry from the University of California, Berkeley. He was a postdoctoral fellow at MIT and a member of the Chemistry faculty at the University of Texas at Austin. Since 1993 he has been at Penn State, where he is now Evan Pugh University Professor and Head of the Department of Chemistry. He is interested in the synthesis of solid state compounds and nanomaterials, and their application to the study of electrochemical and solar energy conversion, catalysis, low-dimensional physical phenomena, and powered motion on the nano- and microscale.